Available online at www.sciencedirect.com
SCIENCE DIRECT®
Combustion and Flame 141 (2005) 89–117
Combustion and Flame
www.elsevier.com/locate/combustflame

Calculations of bluff-body stabilized flames using a joint probability density function model with detailed chemistry

Kai Liu [1], Stephen B. Pope [*], David A. Caughey

Sibley School of Mechanical & Aerospace Engineering, Cornell University, Ithaca, NY 14853, USA

Received 22 June 2004; received in revised form 20 December 2004; accepted 22 December 2004

Abstract

Joint probability density function (PDF) calculations are reported of the bluff-body stabilized flames (HM1, HM2, and HM3) and the results are compared with the available experimental data. The calculations are based on the modeled transport equation for the joint PDF of velocity, turbulence frequency, and composition (species mass fractions and enthalpy) using the interaction by exchange with the mean and Euclidean minimum spanning tree mixing models. The methane chemistry is described by a 19-species augmented reduced mechanism, and is implemented using in situ adaptive tabulation. The numerical accuracy of the calculations is carefully studied, and the associated errors are quantified. For flame HM1 (which has the least local extinction), there is generally good agreement between calculations and measurements, although (for all flames) the quality of the agreement deteriorates at downstream locations. The calculations correctly show essentially inert mixing in the shear layer between the recirculation zone and the coflow in flame HM1, but not in flames HM2 and HM3. In general, the calculations of flames HM2 and HM3 are not in good agreement with the experimental data and do not exhibit the observed local extinction. This deficiency is attributed to the inaccurate calculations of the mean mixture fraction in the recirculation zone (for flames HM2 and HM3). The sensitivity of the calculation to the mixing model constant is investigated, and the mean scalar dissipation is reported.

Keywords: Turbulent combustion; Bluff-body flames; PDF methods

1. Introduction

Bluff-body combustors have been proposed as a test case for turbulent combustion research [1]. Bluff-body stabilized flames have a recirculation zone next to the bluff body that produces a complex turbulent field similar to that commonly found in industrial combustors. Meanwhile, the boundary conditions in these flames are simple and well-defined. Therefore, bluff-body stabilized flames provide an ideal case to investigate the interaction between the turbulence and chemical reaction and provide a good bridge between theoretical problems and engineering applications.

Masri et al. [2–5] and Dally et al. [6–8] have conducted comprehensive experimental investigations on a series of bluff-body flames, from fully burning flames to those exhibiting local extinction. The structure of the flow field and scalar structure, as well

* Corresponding author. 240 Upson Hall, Cornell University, Ithaca, NY 14853, USA. Fax: +1-607-255-1222.
E-mail address: pope@mae.cornell.edu (S.B. Pope).
[1] Present address: Alpha & Omega Semiconductor Inc., 495 Mercury Drive, Sunnyvale, CA 94085, USA.

0010-2180/$ – see front matter
doi:10.1016/j.combustflame.2004.12.018

as chemistry interactions with the turbulence, such as location of the flame, local extinction and reignition, blowoff, and NO_x emission, were investigated. The flames studied in these experiments were selected as target flames for the International Workshop on Measurement and Computation of Turbulent Nonpremixed Flames (TNF). All the experimental data are available online [9].

On the other hand, bluff-body stabilized flames are still a challenging case for turbulent combustion modeling. The challenge is not only due to the complexity of the turbulent flow but also to the complexity of the finite-rate chemistry, which results in high dimensionality and requires computationally intensive integration of the stiff equations of chemical kinetics. Furthermore, the interaction between the turbulent mixing and finite-rate chemical reactions strongly affects the burning of these flames.

Using Sydney bluff-body data as a benchmark for modeling, many researchers have performed simulations of bluff-body flames with different turbulence and/or combustion models. Dally et al. [10] investigated the performance of the k–ε model and Reynolds stress models (RSMs) applied to bluff-body flames and discussed the modification to the constants in the dissipation transport equation and their influence on the prediction of the flow field. Merci et al. [11] investigated the performance of a new cubic nonlinear k–ε model using a preassumed β-probability density function (β-PDF) chemistry model. They found that the influence of the turbulence model on the calculations is substantial, and the cubic nonlinear k–ε model improved the prediction of the flow structure. Li et al. [12] investigated the applicability of existing RSMs to complex flames. They found that most RSMs cannot provide overall satisfactory predictions for this challenging flame. They also found that RSMs behave differently in nonreacting and reacting cases. Equilibrium chemistry and an assumed-shape β-PDF approach were employed for the reacting case. Hossain et al. [13] used the k–ε model with a flamelet model to investigate the effects of heat radiation. They found that the effects of radiative heat transfer on temperature and major species are small for the HM1 flame (a hydrogen and methane flame, see Section 2), but that inclusion of radiative heat transfer effects significantly improves the prediction of OH mass fraction. Kim et al. [14,15] applied the first-order conditional moment closure (CMC) model with GRI2.11 and GRI3.0 mechanisms to bluff-body flames. They demonstrated that the CMC predictions are in good agreement with the measurements for temperature and most major species. The species OH and NO are overpredicted, which may be due to deficiencies in the GRI2.11 and GRI3.0 mechanisms.

In all the above modeling methodologies, the turbulence models are moment closures, and the treatment of chemical reaction is based on mixture fraction. The flames studied show almost no local extinction. Present-day mixture fraction-based models cannot predict local extinction and reignition accurately.

Since the 1980s [16], PDF methods have been well developed and have been demonstrated to be a successful approach to modeling turbulent combustion [17,18]. PDF methods for turbulent reacting flows have the significant advantage that the high-dimensional strongly nonlinear source terms arising from chemical reaction appear in closed form [16]. The approach thus offers an important advantage over single conserved scalar formulations.

Xu and Pope [17] and Tang et al. [19] applied the joint velocity–frequency–composition PDF method to piloted-jet flames. Their results are in good agreement with experimental data not only for profiles and scatterplots, but also for the prediction of local extinction and reignition in these flames. The success of the joint PDF method has benefited from developments in many associated areas, including the implementation of chemistry through in situ adaptive tabulation (ISAT), which tremendously improves the efficiency of the chemistry calculation [20]; the development of the Euclidean minimum spanning tree (EMST) mixing model [21], which successfully describes the main features of turbulent mixing; and the development of the augmented reduced mechanisms (ARM1 [22] and later ARM2 [23]) for methane. Meanwhile, a recently developed, fully consistent, hybrid finite-volume/Monte Carlo particle algorithm dramatically improves the numerical efficiency of the joint PDF method [24,25].

These advances benefit the performance of calculations for complicated flames such as bluff-body stabilized flames. Using the hybrid method, Jenny et al. [26] performed joint PDF calculations for the cold flow in the bluff-body stabilized flame apparatus, and Muradoglu et al. [27] studied bluff-body flames using a simple flamelet model to investigate the sensitivity of the calculations to boundary conditions and model constants. At TNF6 (see [28]) Liu et al. presented results for this flame using a relatively simple skeletal chemical mechanism implemented with ISAT.

Recently, Lindstedt [29] and Kuan [30] performed two-dimensional axisymmetric steady and unsteady calculations for bluff-body stabilized flames with the RSM coupled with the transported composition PDF method. They used the modified curl (MC) mixing model and Lindstedt's reduced methane mechanism [28,29]. Their results for species concentrations (including NO) are far better than the previous results of Reynolds-averaged Navier–Stokes (RANS) calcu-

lations described above, and the flow field remains well reproduced.

This article describes calculations using the joint velocity–frequency–composition PDF method together with the ARM2 mechanism implemented with ISAT to simulate bluff-body flames. The article is structured as follows: In Section 2, the experimental data available (from the University of Sydney) are summarized. In Section 3, a brief review of the current joint velocity–turbulent frequency–composition PDF modeling method is provided. The joint PDF equation, PDF models, and the hybrid FV/particle algorithm are introduced. In Section 4, the Sydney bluff-body stabilized flame burner is described. The details of the calculations are given, including specification of the computational domain, boundary conditions, and numerical parameters. Numerical accuracy issues are investigated using a simple laminar flamelet chemistry model. In Section 5, the joint PDF calculations with the EMST mixing model and the ARM2 reduced mechanism are presented for flames HM1, HM2, and HM3. The results of joint PDF calculations are comprehensively compared with experimental data, including radial mean profiles, conditional means, and scatterplots. The joint PDF models are evaluated. An important property of some combustion models, the mean scalar dissipation rate, $\tilde{\chi}$, is also examined. Finally, in Section 7, conclusions are drawn and suggestions for future work are given.

2. Bluff-body stabilized flames

In the experiments of Masri et al. [4] and Dally [8], a fuel jet is surrounded by a bluff body and a coflowing air stream. The diameter of the bluff body is 0.05 m, and that of the jet is 0.0036 m. There is a recirculation zone immediately next to the bluff-body surface, which stabilizes the flame. Downstream of the recirculation zone is the neck zone, in which there are strong interactions between turbulent mixing and finite-rate chemical reactions. Further downstream there is a jetlike zone. The fuel in these flames (denoted HM) is a mixture of hydrogen (H_2) and either natural gas (CNG, see Table 1) or methane (CH_4) in the volume ratio 1:1.

Experimental data for velocity fields and scalar fields are available. Velocity field data include mean axial velocity, radial velocity, and their variances. The scalar field data consist of means and variances of mixture fraction, temperature, and some major and minor species. These species include O_2, N_2, H_2, H_2O, CO, CO_2, CH_4, OH, and NO. The mixture fraction, ξ, following Bilger's formula [9,31], is defined by

$$\xi = \frac{\frac{2(Z_C - Z_{C,\mathbf{O}})}{W_C} + \frac{Z_H - Z_{H,\mathbf{O}}}{2W_H} - \frac{Z_O - Z_{O,\mathbf{O}}}{W_O}}{\frac{2(Z_{C,\mathbf{F}} - Z_{C,\mathbf{O}})}{W_C} + \frac{Z_{H,\mathbf{F}} - Z_{H,\mathbf{O}}}{2W_H} - \frac{Z_{O,\mathbf{F}} - Z_{O,\mathbf{O}}}{W_O}}, \quad (1)$$

where Z_i is a conserved scalar given by the total mass fraction of element i, W_i is the atomic mass of element i, and the subscripts **F** and **O** refer to the fuel and oxidant streams, respectively.

Table 1 lists the experimental data used in this article, which are available online [9].

Velocity data are provided for flame HM1. The HM1 data are selected because this flame reveals little local extinction so that a simple flamelet model can be used in the calculations to investigate numerical accuracy. In the year 2000, the experiments were repeated by Masri [9] with improved measurement techniques to provide more reliable data for velocity field for the reactive cases, and also to include the covariance of velocity, $\widetilde{uv}$. These data are named HM1E; see Table 1. However, the inlet velocities were slightly different: the bulk jet velocity, U_J, was changed from 118 to 108 m/s, and correspondingly the coflow velocity, U_C, was changed from 40 to 35 m/s. The ratio U_J/U_C was kept the same so that the two flames had almost the same flow structure.

In the series of flames HM1, HM2, HM3, the fuel-jet velocity is varied to investigate the Damkohler number effect on local extinction. The scalar data in each case include Favre-averaged means and variances of the mixture fraction, temperature, and species. Instantaneous scatter data are also available.

Table 1
Experimental data [9]

Case name	Fuel	U_J (m/s)[a]	U_C (m/s)[b]	Year of data	Available data
HM1	CNG[c]:H_2 (1:1)	118	40	1995	$\tilde{U}$, $\tilde{V}$, u'', v''
HM1E	CNG:H_2 (1:1)	108	35	2000	$\tilde{U}$, $\tilde{V}$,
HM3E		195			u'', v'', $\widetilde{uv}$
HM1	CH_4:H_2 (1:1)	118	40	1995	ξ, T, and Y
HM2	$\xi_{st} = 0.050$	178			
HM3		214			

[a] U_J is the jet bulk velocity.
[b] U_C is the coflow velocity.
[c] CNG: 90.9% CH_4, 5.0% C_2H_6, 1.1% C_3H_8, 2.4% CO_2, balance: C_4H_{10} and N_2.

As the jet velocity increases from 118 m/s for HM1 to 214 m/s for HM3 (or from 50% of the blowoff velocity, which is $U_{\mathrm{BL}} = 236$ m/s, to 90% of U_{BL}), the data vary from revealing little local extinction to revealing much local extinction. Recently, HM1E and HM1 data were widely used to compare with various turbulence and combustion modeling calculations [10,11,13,15,27].

3. Joint PDF models

In the joint PDF methodology, a turbulent (nonreactive or reactive) flow is modeled at the level of the one-point, one-time joint PDF of certain fluid properties. At this level, the important processes of convection and chemical reaction are represented exactly without modeling assumptions [16]. In other words, the convection terms and reaction source term in the conservation equations are expressed in exact forms. These advantages overcome the closure problems associated with convection and reaction that arise in traditional statistical approaches and make the joint PDF method an attractive approach for turbulent reactive flows. However, the effects of molecular mixing have to be modeled.

The state of the fluid at any location is fully described by the three components of velocity ($\mathbf{U} = U_1, U_2, U_3$) and by a set of n_ϕ scalars ($\boldsymbol{\Phi} = \phi_1, \phi_2, \ldots, \phi_{n_\phi}$), which are the mass fractions of the ($n_s = n_\phi - 1$) species and the enthalpy. A turbulent reactive flow field can be described by the one-point, one-time joint PDF of the fluid variables, i.e., velocity $\mathbf{U}$, and composition scalars $\boldsymbol{\Phi}$ [25]. Given the one-point, one-time joint PDF, the corresponding statistical quantities of the turbulent reactive flow field can be evaluated as moments of the joint PDF [32]. (Of course, no information is provided about multiple-point, multiple-time statistics.) The one-point, one-time joint PDF of velocity and composition itself does not contain information on the time scales of turbulence; to provide a time scale, the turbulence frequency (defined below) is introduced into the modeled joint PDF equation.

At a given location and time $\{\mathbf{x}, t\}$, $\mathbf{V}$ is the sample space of velocity $\mathbf{U}$, $\boldsymbol{\Psi}$ is the sample space of composition $\boldsymbol{\Phi}$, and θ is the sample space of turbulence frequency ω. The mass density function F and the one-point, one-time Eulerian mass-weighted joint PDF $\tilde{f}$ of velocity $\mathbf{U}(\mathbf{x}, t)$, composition vector $\boldsymbol{\Phi}(\mathbf{x}, t)$, and turbulent frequency $\omega(\mathbf{x}, t)$ are related by [33]

$$
\begin{aligned}
&F(\mathbf{V}, \boldsymbol{\Psi}, \theta; \mathbf{x}, t) \\
&\quad = \langle\rho\rangle \tilde{f}(\mathbf{V}, \boldsymbol{\Psi}, \theta; \mathbf{x}, t) \\
&\quad = \rho(\boldsymbol{\Psi})\big\langle \delta\big(\mathbf{U}[\mathbf{x}, t] - \mathbf{V}\big)\delta\big(\boldsymbol{\Phi}[\mathbf{x}, t] - \boldsymbol{\Psi}\big) \\
&\qquad \times \delta\big(\omega[\mathbf{x}, t] - \theta\big)\big\rangle, \qquad (2)
\end{aligned}
$$

where the tilde and angle brackets denote mass (Favre)-averaged and volume (Reynolds)-averaged means, respectively, and ρ is the fluid density. Similarly, the joint PDF of the fluctuating velocity $\mathbf{u}(\mathbf{x}, t)$ ($\mathbf{v}$ is the sample space of $\mathbf{u}$), composition $\boldsymbol{\Phi}(\mathbf{x}, t)$ and turbulent frequency $\omega(\mathbf{x}, t)$, denoted by $\tilde{g}$, is given by

$$
\begin{aligned}
&\langle\rho\rangle \tilde{g}(\mathbf{v}, \boldsymbol{\Psi}, \theta; \mathbf{x}, t) \\
&\quad = \rho(\boldsymbol{\Psi})\big\langle \delta\big(\mathbf{u}[\mathbf{x}, t] - \mathbf{v}\big)\delta\big(\boldsymbol{\Phi}[\mathbf{x}, t] - \boldsymbol{\Psi}\big) \\
&\qquad \times \delta\big(\omega[\mathbf{x}, t] - \theta\big)\big\rangle. \qquad (3)
\end{aligned}
$$

The exact equation of turbulence frequency is uninformative [34]. Only the exact joint PDF transport equation for velocity and composition is shown here. From [16], the transport equation for joint PDF of velocity and composition can be derived. By subtraction of the mean velocity, the transport equation of fluctuation velocity and turbulence frequency and composition PDF, $\tilde{g}$, can be given as

$$
\begin{aligned}
&\frac{\partial}{\partial t}\big(\langle\rho\rangle\tilde{g}\big) + (\tilde{U}_i + v_i)\frac{\partial}{\partial x_i}\big(\langle\rho\rangle\tilde{g}\big) \\
&\qquad + \left(\frac{\partial \widetilde{u_i u_j}}{\partial x_i} - v_i\frac{\partial \tilde{U}_j}{\partial x_i}\right)\frac{\partial}{\partial v_j}\big(\langle\rho\rangle\tilde{g}\big) \\
&\qquad + \frac{\partial}{\partial \psi_\alpha}\big(\langle\rho\rangle S_\alpha \tilde{g}\big) \\
&\quad = -\frac{\partial}{\partial v_i}\left[\left\langle \frac{\partial \tau_{ij}}{\partial x_j} - \frac{\partial p'}{\partial x_i}\middle|\mathbf{v}\right\rangle \tilde{g}\right] \\
&\qquad + \frac{\partial}{\partial \psi_\alpha}\left[\left\langle \frac{\partial J_i^\alpha}{\partial x_i}\middle|\mathbf{v}, \boldsymbol{\Psi}\right\rangle \tilde{g}\right], \qquad (4)
\end{aligned}
$$

where the angle brackets containing the vertical bar stand for the conditional expectation; S_α is the chemical reaction source term of species α; J_i^α represents the molecular flux of species α in the i direction; τ_{ij} is the viscous stress tensor; and p' is the pressure fluctuation. In the above joint PDF transport Eq. (4), the terms on the left-hand side are in closed form. They represent: evolution in time; transport in the physical space; transport in the velocity space; and transport in the composition space due to reaction, respectively. The terms on the right-hand side need to be modeled. They represent the physical processes of transport in the velocity space due to the viscous stress and pressure fluctuation gradient, and transport in the composition space by the molecular fluxes.

The joint PDF equations are solved by a particle-mesh method, and the modeling can be described most simply in the particle context. In the particle system, $*$ is used to denote particle properties. The general particle has position $\mathbf{X}^*(t)$, velocity $\mathbf{U}^*(t)$, composition $\boldsymbol{\Phi}^*(t)$, and turbulent frequency $\omega^*(t)$. The mean particle velocity at $\mathbf{x}$, $\langle\mathbf{U}^*(t)|\mathbf{X}^*(t) = \mathbf{x}\rangle$, corresponds to the Favre mean velocity $\tilde{\mathbf{U}}(\mathbf{x}, t)$, and

Table 2
Model constants[a]

C_0	$C_{\omega 1}$	$C_{\omega 2}$	C_3	C_4	C_Ω	C_ϕ
2.1	0.56	0.9	1.0	0.25	0.6893	1.5

[a] Note that the effect of C_ϕ is studied in a range of values, i.e., 1.0, 1.5, and 2.0.

similarly for other quantities. The fluctuating velocity of a particle is $\mathbf{u}^*(t) \equiv \mathbf{U}^*(t) - \langle \mathbf{U}^*(t) | \mathbf{X}^*(t) = \mathbf{x} \rangle$.

3.1. Velocity model

The evolution of the fluctuating velocity of a particle can be described by the Langevin equation. Langevin models have been developed at different levels for the velocity of particles [35–37]. Here the simplified Langevin model (SLM) is used:

$$du_i^*(t) = \frac{1}{\langle\rho\rangle}\frac{\partial(\langle\rho\rangle\widetilde{u_i u_j})}{\partial x_j}\,dt - u_j^*\frac{\partial \tilde{U}_i}{\partial x_j}\,dt - \left(\frac{1}{2}+\frac{3}{4}C_0\right)\Omega u_i^*(t)\,dt + (C_0\tilde{k}\Omega)^{1/2}\,dW_i. \quad (5)$$

$\mathbf{W}$ is an isotropic Wiener process; Ω is the conditional mean turbulence frequency, which is defined below; $\tilde{k} \equiv \frac{1}{2}\widetilde{u_i u_j}$ is the Favre mean turbulent kinetic energy; and C_0 is a model constant (see Table 2). The SLM is equivalent to the Rotta model at the second moment closure level [36].

3.2. Turbulence frequency model

The stochastic model for particle turbulence frequency $\omega^*(t)$ is the Jayesh–Pope model [37],

$$d\omega^*(t) = -C_3(\omega^* - \tilde{\omega})\Omega\,dt - S_\omega\Omega\omega^*(t)\,dt + \left[2C_3C_4\tilde{\omega}\Omega\omega^*(t)\right]^{1/2}dW, \quad (6)$$

where W is an independent Wiener process. To account for external intermittency effects, the conditional mean turbulence frequency Ω is defined by

$$\Omega \equiv C_\Omega\frac{\langle\rho^*\omega^*|\omega^* \geqslant \tilde{\omega}\rangle}{\langle\rho\rangle}, \quad (7)$$

where the model constant C_Ω is chosen such that Ω and $\tilde{\omega}$ are equal in fully developed homogeneous turbulence (Table 2). In Eq. (6), S_ω is the source term defined as

$$S_\omega = C_{\omega 2} - C_{\omega 1}\frac{\mathcal{P}}{\tilde{k}\Omega}, \quad (8)$$

where $\mathcal{P}$ is the rate of turbulence production,

$$\mathcal{P} = -\widetilde{u_i u_j}\frac{\partial \tilde{U}_i}{\partial x_j}, \quad (9)$$

and C_3, C_4, $C_{\omega 1}$, and $C_{\omega 2}$ are model constants. The values of these constants are specified in Table 2.

The mean rate of dissipation $\tilde{\varepsilon}$ of turbulent kinetic energy $\tilde{k}$ is modeled by

$$\tilde{\varepsilon} = \tilde{k}\Omega. \quad (10)$$

This equation provides the connection between the modeled turbulent frequency ω^* and physical quantities. Including the turbulence frequency as a particle property of the modeled stochastic particles provides a time scale of turbulence that can be used in joint PDF modeling.

3.3. Mixing models

The effects of molecular diffusion are represented by a mixing model. Several mixing models have been proposed for PDF calculations, including the interaction by exchange with the mean (IEM) model [38], the modified Curl (MC) mixing model [39], and the Euclidean minimum spanning tree (EMST) mixing model [21]. Mixing models are crucial in joint PDF calculations of turbulent nonpremixed flames with finite-rate chemical reactions. In this study, the IEM and EMST mixing models are used in joint PDF calculations of bluff-body stabilized flames, and comparisons are made between the results of calculations using these two mixing models. None of the mixing models mentioned above takes into account the effect of differential diffusion.

3.3.1. IEM mixing model

In the IEM model, the composition of the particles evolves by an ordinary differential equation,

$$d\phi^*(t) = -\frac{1}{2}C_\phi\Omega\left(\phi^*(t) - \tilde{\phi}\right)dt, \quad (11)$$

where C_ϕ is a model constant specified in Table 2.

3.3.2. EMST mixing model

The EMST mixing model is a complicated particle-interaction model, designed to overcome shortcomings of simpler models. In addition to the particle composition $\Phi(t)$, the model involves a state variable $s(t)$. A full description of the EMST model can be found in [21,40]. In short, at any time the model chooses a subset of N_s particles to mix from the ensemble of N_{pc} particles in a grid cell according to the mixing history of each particle recorded by the state variable $s(t)$. A Euclidean minimum spanning tree is formed in the composition space on this subset of N_s particles, so that each particle is associated with at least one neighboring particle. The mixing evolves the compositions of these N_s particles (for $i = 1, \ldots, N_s$)

by

$$w^{(i)}\frac{d\phi_\alpha^{(i)}}{dt} = -\gamma \sum_{\nu=1}^{N_s-1} B_\nu \big[\big(\phi_\alpha^{(i)} - \phi_\alpha^{(n_\nu)}\big)\delta_{im_\nu} + \big(\phi_\alpha^{(i)} - \phi_\alpha^{(m_\nu)}\big)\delta_{in_\nu}\big], \quad (12)$$

where $w^{(i)}$ is the numerical particle weight, m_ν and n_ν are the indexes of the two particles connected by the EMST edge ν, B_ν is a model coefficient discussed in [21], δ_{ij} is the Kronecker delta, and γ is determined such that the composition variance decays at a specified rate. The decay rate is controlled by the mixing time scale τ_ϕ, which is modeled by [41]

$$\tau_\phi = \frac{\tau}{C_\phi}, \quad (13)$$

where τ is the turbulence time scale given by

$$\tau \equiv 1/\Omega, \quad (14)$$

and C_ϕ is an empirical constant that can be interpreted as the velocity-to-scalar time scale ratio. Changing C_ϕ changes the mixing time scale and, thus, changes the decay rate. The effects of changing C_ϕ are discussed in Section 5.

The EMST model is a localized mixing model that has been successfully used in previous joint PDF calculations of piloted-jet turbulent nonpremixed flames [19,42] to predict local extinction and reignition.

3.4. Mixture fraction/flamelet model

A simple flamelet model is used for the investigation of numerical accuracy to reduce the computational work, instead of the more advanced models used for the main part of the investigation. For this simple flamelet model, the thermochemical properties are functions of only one variable, the mixture fraction ξ. The definition of mixture fraction ξ follows the Bilger formula, which is the same as that used in the experimental data [9], Eq. (1).

The flamelet table for the simple flamelet model is generated [43] by laminar flame calculations using the GRI2.11 mechanism, which has 49 species. Differential diffusion is taken into account. The strain rate is 100 s^{-1}, the fuel is CH_4:H_2 in the volume ratio 1:1. The initial temperature is 300 K, and the initial pressure is 1 atm.

3.5. Detailed chemistry model

Sung et al. [23] derived an augmented reduced mechanism (ARM) from the GRI2.11 mechanism. The first version, namely, ARM1, includes 16 species and 12 reaction steps: C_2 species are included to improve the prediction of CO. The ARM1 mechanism is extended by including a description of NO_x formation, which results in an augmented reduced mechanism of 19 species and 15 reaction steps, namely, ARM2. The ARM1 and ARM2 mechanisms are available on the web site of the TNF workshop [28]. Both ARM1 and ARM2 were successfully used in previous joint PDF calculations of piloted-jet flames [17,19].

In joint PDF calculations it is possible to implement an accurate detailed mechanism, such as the GRI2.11 mechanism. However, reduced mechanisms such as ARM2 are more attractive for turbulent combustion simulations, because they are considerably less expensive compared with GRI2.11, and according to previous calculations, they are equally accurate. ARM2 is used in the current joint PDF calculations, implemented using the ISAT algorithm [20].

4. Numerical method and accuracy

For a general three-dimensional flow, the joint PDF is a function of at least seven independent variables (three position variables, three velocity components, and turbulent frequency), plus the number of chemical species from the chemistry mechanism included in the joint PDF equations to be solved. As a result, it is computationally prohibitive to solve the joint PDF transport equation using conventional numerical techniques such as finite-difference and finite-element methods. However, Monte Carlo particle-mesh methods provide an efficient way to solve the high-dimensional equation. The joint PDF of fluid properties is represented by a large number of stochastic particles, which are randomly and continuously distributed in the flow domain, which is covered by a mesh. The stochastic particle properties evolve according to a set of modeled stochastic differential equations (SDEs) such that the PDF of particle properties evolves as the modeled PDF transport equation.

In this study, a fully consistent hybrid finite-volume/Monte Carlo particle algorithm is used to solve the joint PDF equation [25,44]. The conservation equations for mean mass, momentum, and energy, coupled with a mean equation of state, are derived directly from the joint PDF transport equation and solved by an efficient FV method, while a particle-mesh-based Monte Carlo algorithm is employed to solve the modeled transport equation of the joint PDF for fluctuating velocity, turbulent frequency, and compositions. It is emphasized that the present hybrid method is completely consistent at the level of equations solved by the FV and the particle algorithms [25]. Correction algorithms have been developed to make the hybrid method fully consistent also at the numerical solution level [25]. Compared with the previous stand alone particle algorithm, by

use of a smooth mean velocity field in the particle SDEs, this hybrid algorithm substantially reduces the bias error.

One of the important issues in numerical simulations is the numerical accuracy of the calculated results. The accuracy of the numerical simulations of complex turbulent flames depends mainly on two factors: the physical models, including turbulence and chemistry models; and the numerical solution algorithm. To investigate the numerical errors in the solution algorithms and understand the flow structure, we use the simple chemistry model described in Section 3, in which all the chemistry properties, including density, temperature, and mass fraction of species, are functions of only one variable, the mixture fraction, ξ. For the same purpose, the simple IEM mixing model is used in most of the calculations in this section, except for the investigation of bias errors, in which the EMST mixing model is used.

Xu and Pope [17] and Jenny et al. [26] investigated the numerical errors involved in joint PDF calculations. There are three kinds of numerical errors in the current joint PDF algorithm: statistical errors, discretization errors, and bias errors; the last two can be categorized as deterministic errors.

4.1. Solution domain

A polar-cylindrical coordinate system (x, y, θ) is adopted for the present calculations. The origin of the coordinate system is on the centerline ($y = 0$) at the jet exit plane ($x = 0$). Here, x and y represent the axial and radial directions, respectively. The computational domain is taken to be a rectangle in the plane $\theta = 0$ with two sides, 0.36 m ($7.2D_B$) in the axial direction and 0.15 m ($3D_B$) in the radial direction, where $D_B = 0.05$ m is the diameter of the bluff body. Fig. 1 is a sketch of the solution domain. The treatment of boundaries in the current code does not allow the inflow boundary to be upstream of the plane of the bluff body.

4.2. Boundary conditions

The boundary conditions are well defined for bluff-body flows. For the particle part, the boundary conditions on the four boundaries are described below.

The coflow boundary ($y = 3D_B$) is treated as an impermeable perfect-slip wall. Computational particles are reflected from the boundary without change in their properties (except for the reflection of the radial velocity). At the exit plane, $x = 7.2D_B$, outflow boundary conditions are applied. When particles cross the boundary, they are eliminated. Symmetry conditions are applied on the axis $y = 0$. Particles never

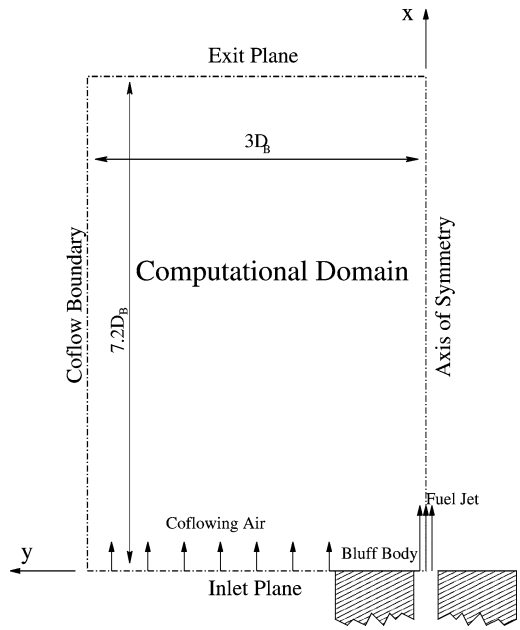

Fig. 1. Sketch of the computational domain (not to scale).

cross the axis, and so no boundary conditions are required on the particle properties. The mean fields are forced to satisfy the symmetry conditions. The radial derivative of the mean axial velocity and of the turbulence kinetic energy are forced to be zero. The mean radial velocity $\tilde{U}_2$ is zero.

At the inlet plane $x = 0$, there are three regions: from $y = 0$ to $y = R_J$ (R_J is the radius of the jet) is the jet where the fuel flows in; from $y = R_J$ to $y = R_B$ (R_B is the radius of the bluff body) is the bluff-body surface; and from $y = R_B$ to $y = 6R_B$ (the coflow boundary) is the coflow region where air flows in. In the two inflowing streams, the particles flow in with a specified distribution of properties. In detail, the velocities have a joint normal distribution and the frequency has a gamma distribution, all with specified statistical properties (see [33] for details). The means are shown in Fig. 2 and explained later.

In the bluff-body region, the face of the bluff body is treated as a perfect-slip wall. Particles reflect at the wall without a change in their properties, except that the axial velocity changes sign. The influence of the perfect-slip boundary condition (in comparison to the alternative "wall-function" boundary condition) has not been investigated, but is thought not to be large.

4.2.1. Mean velocities

In the jet region, the power law profile is applied as

$$\widetilde{U_1(y)} = C_U U_J \left(C_c - \frac{y}{R_J} \right)^p, \tag{15}$$

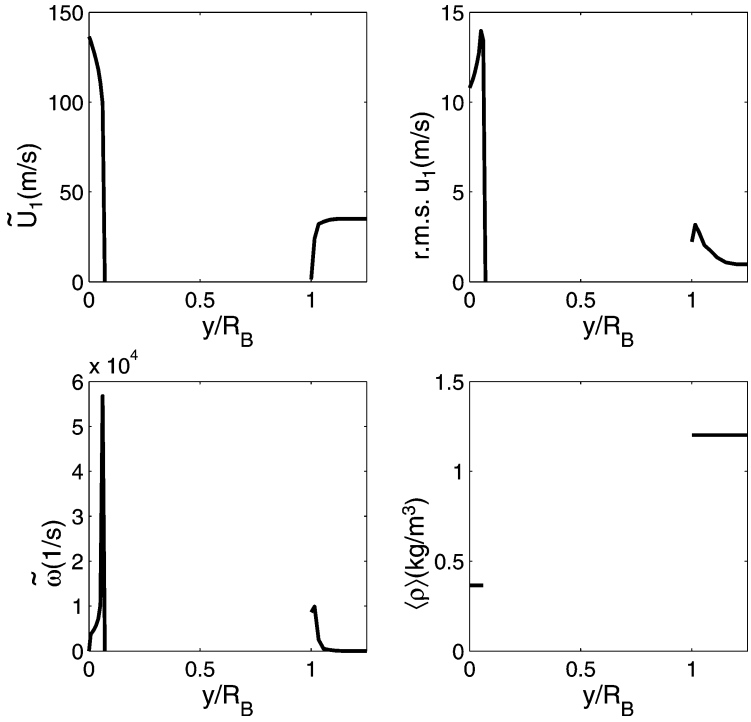

Fig. 2. Specified inlet boundary conditions for flame HM1E. Zero-normal gradient boundary conditions are applied on the bluff-body surface ($R_{\mathrm{Jet}} < y < R_{\mathrm{B}}$).

where U_{J} is the jet bulk velocity, and R_{J} is the radius of jet. In parentheses, $C_{\mathrm{c}} = 1.01$ is used instead of 1.0 to avoid the singularity of the derivative of mean velocity at the wall of the jet; p is the profile exponent, set at 1/6 here; C_{U} is the normalization constant, which is determined by the condition that the area averaged velocity given by Eq. (15) is the specified bulk velocity U_{J}. Therefore, C_{U} satisfies

$$C_{\mathrm{U}} = \frac{(2+p)(1+p)}{2}\big[C_{\mathrm{c}}^{2+p} - (C_{\mathrm{c}} - 1.0)^{2+p} - (2+p)(C_{\mathrm{c}} - 1.0)^{1+p}\big]^{-1}, \tag{16}$$

and C_{c} is set at 1.01 as explained above.

The mean radial and circumferential velocities are set to zero.

In the coflow region, the inlet boundary condition on $\tilde{U}_1$ is obtained from interpolation of the experimental data [9] in the coflow region; Lagrangian third-order interpolation is used.

The other components of the mean velocity are zero.

4.2.2. Variances and covariance of velocity

The inlet boundary condition on the Favre-averaged variance $\widetilde{u_1^2}$ is interpolated from the experimental data. The other two normal components of the variances (which are not available from the data) are set equal to $\widetilde{u_1^2}$ following the suggestion of [9]. And the covariance is specified as

$$\widetilde{u_1 u_2} = \rho_{12}\big(\widetilde{u_1^2}\widetilde{u_2^2}\big)^{1/2} = \rho_{12}\widetilde{u_1^2}, \tag{17}$$

where ρ_{12} is the correlation coefficient, and the value $\rho_{12} = 0.5$ is recommended by Masri [9]. Here it is specified as

$$\rho_{12} = \begin{cases} C_{\mathrm{cv}}\frac{y}{R_{\mathrm{J}}}, & y \leqslant R_{\mathrm{J}}, \\ -C_{\mathrm{cv}}, & y \geqslant R_{\mathrm{B}}, \end{cases} \tag{18}$$

and C_{cv} is set at 0.5. For this axisymmetric flow with no mean swirl, $\widetilde{u_1 u_3}$ and $\widetilde{u_2 u_3}$ are zero.

4.2.3. Turbulence frequency $\tilde{\omega}$

The calculation results are very sensitive to the inlet boundary condition on turbulence frequency, $\tilde{\omega}$, but no experimental data are available. According to the definition of turbulence frequency and the relation of the fully developed turbulence at the inlet boundary, the following formula is used to set $\tilde{\omega}$ at the inlet boundary:

$$\tilde{\omega} = \frac{\tilde{\varepsilon}}{\tilde{k}} = \frac{1}{C_P}\frac{\mathcal{P}}{\tilde{k}} = -\frac{1}{C_{\mathrm{P}}}\frac{\widetilde{u_1 u_2}}{\tilde{k}}\frac{d\tilde{U}_1}{dy}. \tag{19}$$

$\tilde{\varepsilon}$ is the mean dissipation rate, $\tilde{k}$ is the kinetic energy, $\mathcal{P}$ is production, and C_{P} is the ratio of production to dissipation. Here, $C_{\mathrm{P}} = 1.0$ is used.

The simulation results are not sensitive to the velocity profile exponent, p, nor to the correlation coefficient, ρ_{12}, within reasonable ranges.

4.3. Time averaging factors and statistical stationarity

Time averaging is an important technique used to reduce statistical errors in particle simulations. The time averaging method used here follows Ref. [25]:

$$Q_{\mathrm{TA}}^{k} = \left(1 - \frac{1}{N_{\mathrm{TA}}}\right) Q_{\mathrm{TA}}^{k-1} + \frac{1}{N_{\mathrm{TA}}} Q^{k}. \tag{20}$$

Q_{TA}^{k} and Q^{k} are the time-averaged and instantaneous values of property Q evaluated at the kth particle time step, respectively. The parameter N_{TA} is the time-averaged factor to be specified.

There are three categories of fields to be time-averaged. The first category consists of the fields used within the particle part: the time averaging factor for this category is denoted as N^{P}. The second category consists of the particle fields passed to the finite-volume solver: this time averaging factor is denoted as N^{P2FV}. The last category consists of finite-volume fields, for which the time averaging factor is denoted by N^{FV}. Because the finite-volume solver is not fully converged at each outer iteration (between the particle part and the finite-volume solver), time averaging is still needed for the finite-volume fields.

The time averaging factors are increased as the calculations proceed. The strategy for increasing the time averaging factors in this article is different from that in [25]; see [45] for details. As far as the statistically stationary states are concerned, only the final parameters are relevant. Here the final time averaging factors used are the same as those in [27], and are listed in Table 3.

The current hybrid method is designed to simulate only statistically stationary flows. Therefore, the achievement of statistical stationarity is examined. Time-averaged mean velocity fields and mean density, as well as the mass fractions of species, at several monitoring locations are monitored and shown to reach statistically stationary values. For calculations with the flamelet model, about 6000 to 9000 particle time steps are needed to reach the statistically stationary state. Generally, 6000 additional particle time steps are taken to make sure that the statistically stationary state is maintained long enough for time averaging. Using the flamelet calculations as initialization fields, it takes about 3000 particle steps for the calculations with the ARM2 mechanism to reach the statistically stationary state. Then, an additional 3000 particle time steps are taken for the reasons given above.

Table 3
Time averaging factors

	N^{P}	N^{P2FV}	N^{FV}
Final value (N_{TA})	500	5	20

4.4. Grid convergence

One of the numerical errors in the joint PDF algorithm is the spatial discretization error. The spatial discretization error results from the spatial discretization in the finite-volume method and also from the kernel estimation and interpolation schemes in the particle algorithm due to the finite size of the grid cells. Xu and Pope [17], Jenny et al. [26], and Muradoglu et al. [27] have extensively investigated spatial discretization errors in the joint PDF method. It has been shown that the current joint PDF algorithm is second-order accurate in space. In this section, an extensive study is not repeated; instead, grid convergence is demonstrated.

Nonuniform rectangular grids are distributed in the computational domain (Fig. 1). The grids used in the current work are different from those used in the previous work [27]; the current grids are more concentrated in the recirculation zone and neck zone in the axial direction, and are more concentrated in the jet region and in the shear layer between the outer edge of the bluff body and the coflow in the radial direction. The details of the grids used in this section are listed in Table 4. It is found that to obtain numerically accurate results with a given number of grid cells (or, equivalently, the same computational cost), it is crucial to distribute more grid lines in the radial direction than in the axial direction. On the other hand, the resulting larger-aspect-ratio cells adversely affect the iterative convergence of the solution. Therefore, the distribution of grids has to be a compromise between these two considerations. The maximum aspect ratio of the cells in the grids used here is less than 40.

Flame HM1E (see Table 1) is selected as the test case to investigate grid convergence. The four grids used in this study are characterized in Table 4. Except for the grids, all other numerical parameters in the calculations are the same, including the number of particles per cell, $N_{\mathrm{PC}} = 25$. The time-averaged profiles are shown in Fig. 3 for axial velocity $\tilde{U}_1$, r.m.s. of axial fluctuating velocity u_1'', mean mixture fraction $\tilde{\xi}$, and r.m.s. of the mixture fraction fluctuation ξ''. The profiles are shown at the axial location of $x/D_{\mathrm{B}} = 0.6$. The discrepancies are small at most locations for the mean fields on the three finest grids. On the other hand, the profiles of variances are more sensitive to the grid size. The results on the coarsest

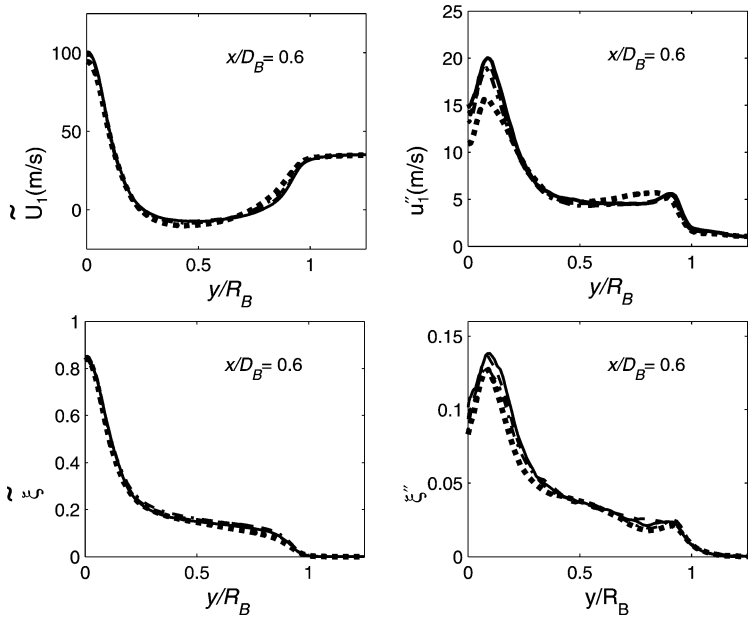

Fig. 3. Grid convergence studies: radial profiles at $x/D_B = 0.6$ of the mean and r.m.s. axial velocity and mixture fraction. Solid line: Grid A; dashed line: Grid B; dash-dotted line: Grid C; dotted line: Grid D.

Table 4
Grids used for grid convergence study

	Grid A	Grid B	Grid C	Grid D
N_X	120	96	72	48
N_Y	160	128	96	64
Zone 1[a]	21	17	13	8
Zone 2[b]	28	22	17	11
Zone 3[c]	87	69	52	35

[a] Grids distributed in jet and first shear layer in radial direction $y/R_B \leqslant 0.144$.

[b] Grids distributed in second shear layer in radial direction $0.8 \leqslant y/R_B \leqslant 1.2$.

[c] Grids distributed in recirculation and neck zone in axial direction $x/D_B \leqslant 3.0$.

grid, Grid D, have obvious discrepancies with the results on the three finer grids.

Fig. 4 shows the time-averaged mean values against $M^{-2} = (N_X \times N_Y)^{-1}$ at selected locations. These locations are selected within the shear layer between the jet and the recirculation zone where the largest discrepancies are observed between the profiles in Fig. 3. For mean axial velocity $\tilde{U}_1$ and mean mixture fraction $\tilde{\xi}$, the plots against M^{-2} show an approximately linear relationship for results on the three finer grids, Grids A, B, and C. This linear behavior is consistent with second-order spatial accuracy. The converged value of these means is estimated by extrapolating to $M^{-2} = 0$. The error between the values of $\tilde{U}_1$ and $\tilde{\xi}$ and the accurate (extrapolated) values is generally less than 3% on Grid A and 10% on Grid C. For the most part, the r.m.s. values of axial velocity and mixture fraction against M^{-2} also show a linear relationship. The error between the calculated values of ξ'' and the accurate values is less than 4% on Grid A and 12% on Grid C. The error for u_1'' is less than 10% on Grid A and 20% on Grid C. Considering the computational cost of the detailed chemistry calculations, the discrepancy between the results on Grid C and those on the finer grid (Grids A and B) is acceptable for the current flame calculations. Therefore, Grid C (with 72 cells in the axial direction and 96 cells in the radial direction) is used in the following calculations. On this grid the spatial discretization error is estimated to be no more than 10% for mean quantities and 20% for r.m.s. quantities.

4.5. Bias

Bias error is a deterministic numerical error caused by using a finite number of particles and is expected to scale as N_{PC}^{-1} [46], where N_{PC} is the number of particles per cell. The bias error in the joint PDF method has been extensively studied in [26,27,46]. It was found that, although bias error is one of the major numerical errors in the previous standalone joint PDF methods [46], it has been dramatically reduced in the current hybrid FV/Monte Carlo algorithm [25,26]. Such extensive studies are not repeated in the current work. The IEM mixing model was used in all previous studies of bias errors in the joint PDF method. However, the EMST mixing model is regarded as a

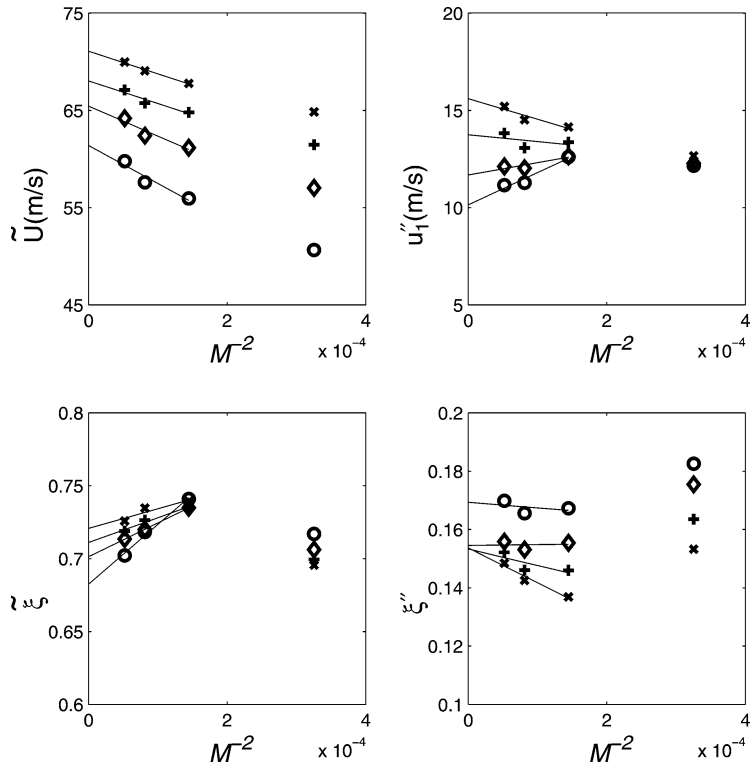

Fig. 4. Time-averaged mean quantities against M^{-2} ($M^2 = N_X \times N_Y$) on the four grids at selected locations: ∘, $(x, y) = (0.6D_B, 1.0R_J)$; ⋄, $(0.9D_B, 1.0R_J)$; +, $(1.3D_B, 1.0R_J)$; ×, $(1.8D_B, 1.0R_J)$.

successful mixing model for piloted-jet flames [17] and is used with detailed chemistry in the current bluff-body stabilized flame calculations, i.e., HM1, HM2, and HM3. The behavior of bias errors for calculations with the EMST mixing model is studied here.

For this purpose, the HM1 flame is selected as the test case. Calculations are performed with different values of N_{PC}, i.e., 25, 50, 100, 200, and 400, on the same grid, Grid C. When a small number of particles per cell is used, for example, $N_{PC} = 25$, many cells do not have enough particles to participate in the mixing required in the EMST mixing model at each time step and it is necessary to skip the mixing step. Even with 50 particles per cell, there are several cells that fail to do EMST mixing on some time steps. So it is unreliable to use a value of N_{PC} less than 50 with the EMST model for the current bluff-body flame calculations.

The time-averaged radial profiles of $\tilde{U}_1$, u_1'', $\tilde{\xi}$, and ξ'' are shown in Fig. 5. Except for the results with $N_{PC} = 25$, the differences between the radial profiles with different values of N_{PC} are very small, which means that the bias errors are small and negligible. To quantify the bias errors, Fig. 6 shows the time-averaged mean values against N_{PC}^{-1} at selected locations (results with $N_{PC} = 25$ are not included). These selected locations are chosen within the first shear layer, which is between the jet and the recirculation zone. Again, the converged values of these means are estimated by extrapolating to $1/N_{PC} = 0$ (or $N_{PC} = \infty$). The dashed lines represent a ±5% interval relative to the extrapolated values. The results show that, except for $N_{PC} = 50$ at several locations, all time-averaged mean values are within 5% at the selected locations. The value $N_{PC} = 100$ is used in the following ARM2 calculations with the EMST mixing model.

4.6. ISAT error tolerance

The ISAT algorithm, developed by Pope [20], is a storage/retrieval technique for the calculation of composition changes due to chemical reaction. The accuracy of the ISAT algorithm depends on a specified ISAT absolute error tolerance, ε_{tol}, which controls the error in the tabulation and, therefore, controls the error incurred in retrieving from the ISAT table. It is very difficult to perform detailed testing on the accuracy of ISAT with real flame calculations due to the large computational cost.

Alternatively, a simple test case, autoignition, is designed to study the accuracy of ISAT for the HM flame calculations. Autoignition is a purely chemical

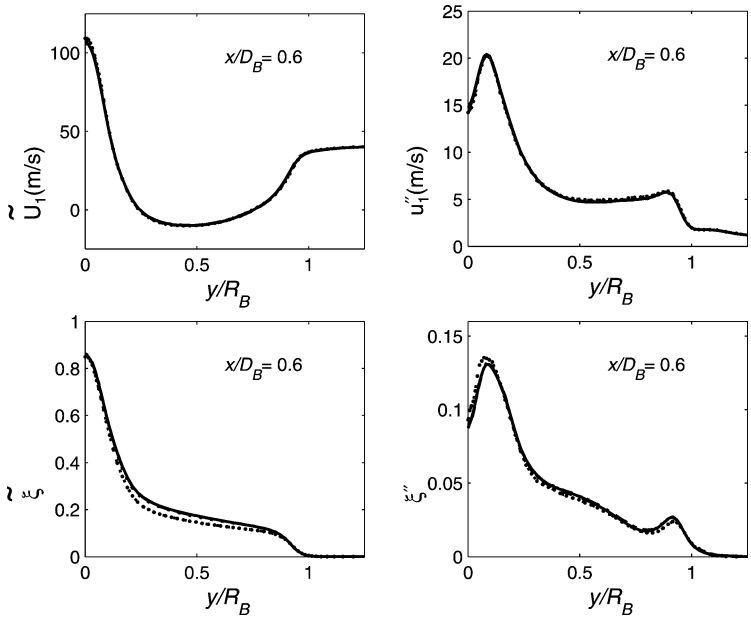

Fig. 5. Bias error studies: radial profiles at $x/D_{\mathrm{B}} = 0.6$ of the mean and r.m.s. axial velocity and mixture fraction. Solid line: $N_{\mathrm{pc}} = 400$; dashed line: $N_{\mathrm{pc}} = 200$; dash-dotted line: $N_{\mathrm{pc}} = 100$; dotted line: $N_{\mathrm{pc}} = 50$; dots: $N_{\mathrm{pc}} = 25$.

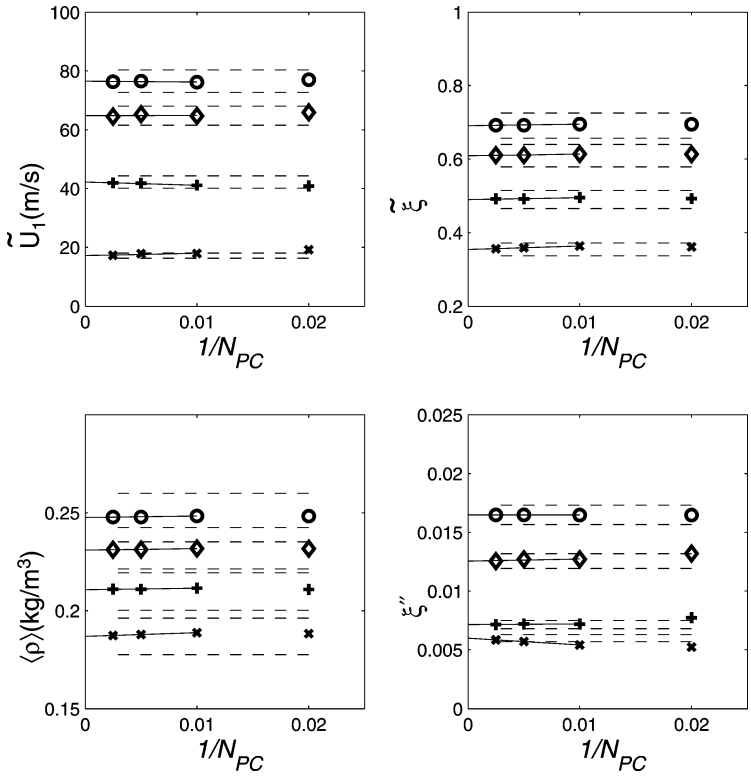

Fig. 6. Time-averaged mean quantities against N_{PC}^{-1} at the selected locations: ∘, $(x, y) = (0.6D_{\mathrm{B}}, 1.0R_{\mathrm{J}})$; ⋄, $(0.9D_{\mathrm{B}}, 1.0R_{\mathrm{J}})$; +, $(1.3D_{\mathrm{B}}, 1.0R_{\mathrm{J}})$; ×, $(1.8D_{\mathrm{B}}, 1.0R_{\mathrm{J}})$. The dashed lines indicate a ±5% error interval about the "accurate" values corresponding to $N_{\mathrm{PC}} = \infty$.

process in which a given mixture of fuel and oxidant at a specified initial temperature and constant pressure reacts and eventually reaches chemical equilibrium. The purpose of studying the accuracy of ISAT using autoignition is to mimic the conditions of the chemical reaction substep in the bluff-body HM flame calculations, including the temperature, T, mixture fraction, ξ, and time step, Δt. Thus, the initial condition of autoignition, i.e., initial mixture fraction and temperature, and all the following time steps are selected carefully to mimic the conditions in real flame calculations. Note that this is not a strict study of numerical accuracy for real flame calculations, but rather serves to provide a reference for parameter determination.

Many cases with other initial conditions were also investigated but are not reported here. The three conditions selected show the greatest sensitivity to the numerical error tolerance parameter ε_{tol}. The variable time stepping technique is used in the current joint PDF calculations. In the autoignition test, variable time steps Δt are randomly distributed uniformly between 8.0×10^{-7} and 8.0×10^{-5} (s), which is

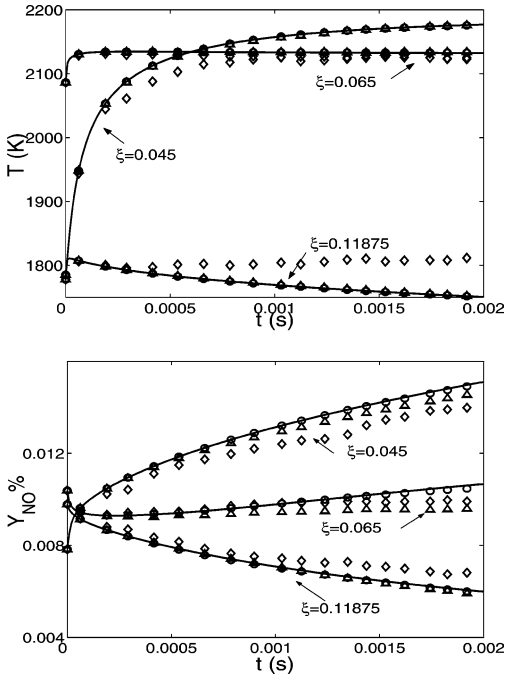

Fig. 7. Investigation of ISAT performance using autoignition: temperature and mass fraction of NO against time for different values of ε_{tol}. Line, direct integration; ∘, $\varepsilon_{\text{tol}} = 10^{-5}$; △, $\varepsilon_{\text{tol}} = 10^{-4}$; ⋄, $\varepsilon_{\text{tol}} = 10^{-3}$.

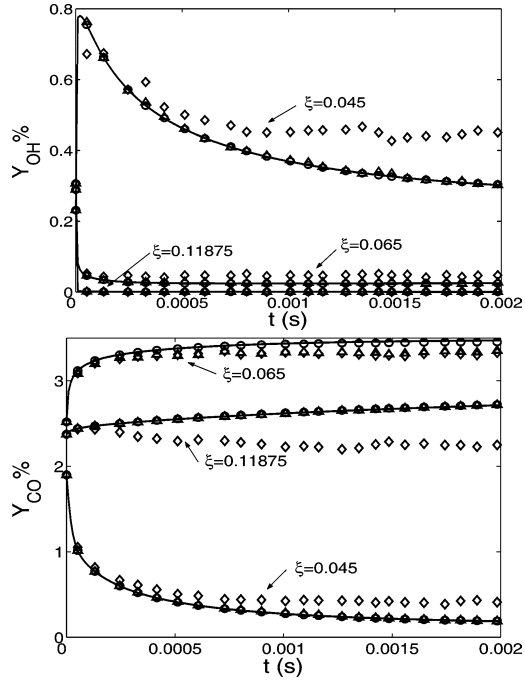

Fig. 8. Investigation of ISAT performance using autoignition: mass fraction of OH and CO against time for different values of ε_{tol}. Line, direct integration; ∘, $\varepsilon_{\text{tol}} = 10^{-5}$; △, $\varepsilon_{\text{tol}} = 10^{-4}$; ⋄, $\varepsilon_{\text{tol}} = 10^{-3}$.

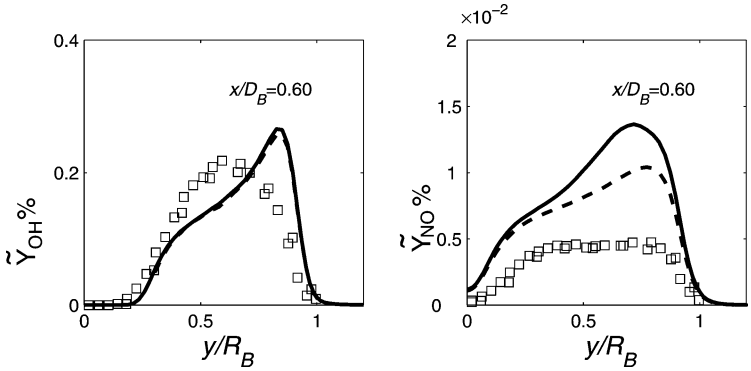

Fig. 9. Investigation of ISAT performance in PDF calculations of flame HM3. Radial profiles at $x/D_{\text{B}} = 0.60$ of the mean mass fractions of OH and NO: Symbols, experimental data [9]; solid lines, $\varepsilon_{\text{tol}} = 10^{-4}$; dashed lines, $\varepsilon_{\text{tol}} = 0.25 \times 10^{-4}$.

the same range of time steps used in the bluff-body flame calculations. The same variable-time-step series is used in each of the runs with different values of mixture fraction ξ and error tolerance ε_{tol}.

The effects of the tabulation error tolerance ε_{tol} are shown in Figs. 7 and 8. Results from direct integration are used as a benchmark for comparison. The results from three error tolerances $\varepsilon_{\text{tol}} = 10^{-3}$, 10^{-4}, and 10^{-5} are included in the figures. Apparently, $\varepsilon_{\text{tol}} = 10^{-3}$ cannot guarantee accuracy of the ISAT tabulation. The results with $\varepsilon_{\text{tol}} = 10^{-4}$ are accurate for temperature and all the major species (not shown here). The maximum errors in these quantities are less than 1%. The maximum errors of CO and OH (with $\varepsilon_{\text{tol}} = 10^{-4}$) are less than 5%. Species NO is slow to reach equilibrium. With $\varepsilon_{\text{tol}} = 10^{-4}$, the maximum error is less than 10%.

One test case for the HM3 flame is performed with the smaller ISAT tabulation error tolerance $\varepsilon_{\text{tol}} = 0.25 \times 10^{-4}$ to test the accuracy of ISAT in a full flame calculation. Radial profiles of the mean mass fraction of OH and NO are shown in Fig. 9. The differences in species OH are negligibly small. Also the differences in the profiles of temperature, major species, and species CO (not shown here) are negligibly small. The differences in the profiles of NO are significant. At $x/D_{\text{B}} = 0.6$, the difference in the calculations of $\widetilde{Y}_{\text{NO}}$ is as large as 30%.

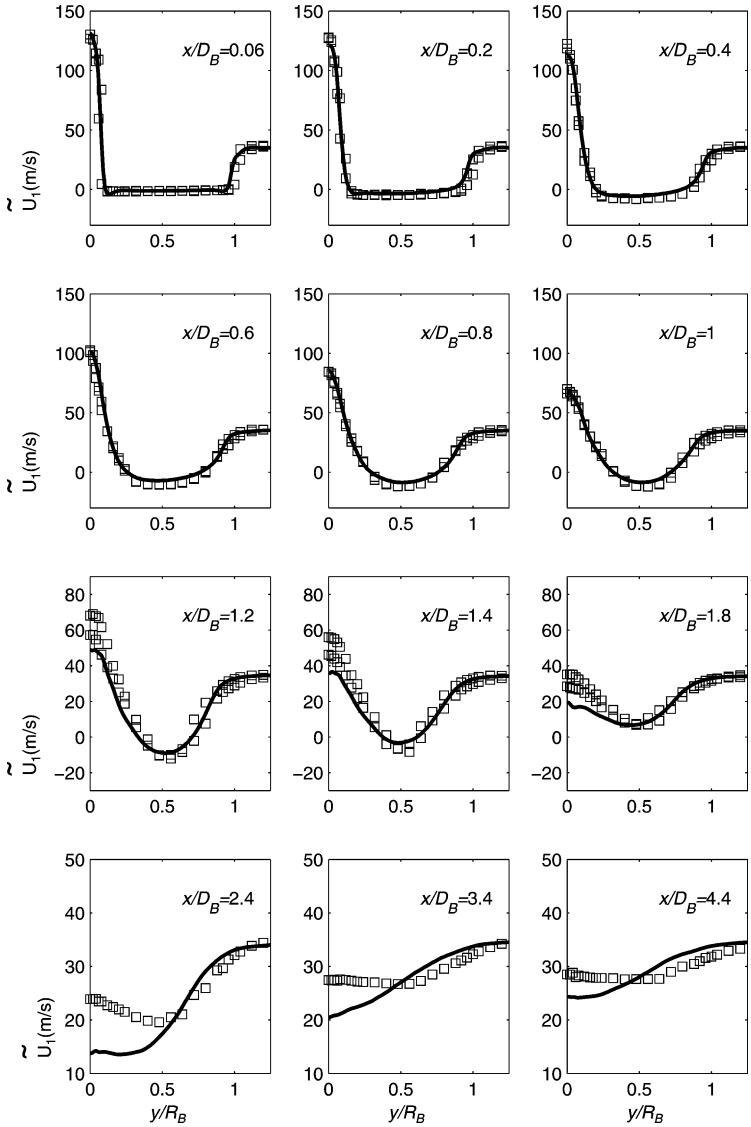

Fig. 10. Radial profiles of the mean axial velocity $\tilde{U}_1$. Symbols, experimental data [9]; lines, joint PDF calculations with IEM mixing model and flamelet chemistry model.

From the above observations, we conclude that the ISAT error tolerance $\varepsilon_{\text{tol}} = 1.0 \times 10^{-4}$ guarantees good accuracy for all species except NO. The value $\varepsilon_{\text{tol}} = 10^{-4}$ is used in the calculations in the following section.

5. Results

5.1. Velocity field

The velocity fields from the joint PDF calculations are compared with the experimental data for flame HM1E, as these data are recommended by the experimentalist [28]. Calculations have been performed with the SLM velocity model, the JPM turbulent frequency model, the IEM mixing model, and the flamelet chemistry model. (Here, the comparison is focused on the velocity fields. Therefore, the IEM mixing model is used.)

The radial profiles of the time-averaged mean velocities $\tilde{U}_1$ and $\tilde{U}_2$, and r.m.s. velocities u_1'' are shown together with the experimental data in Figs. 10–12. Generally, the agreement between the joint PDF calculations and the experimental data is good at upstream locations, which are within the recirculation

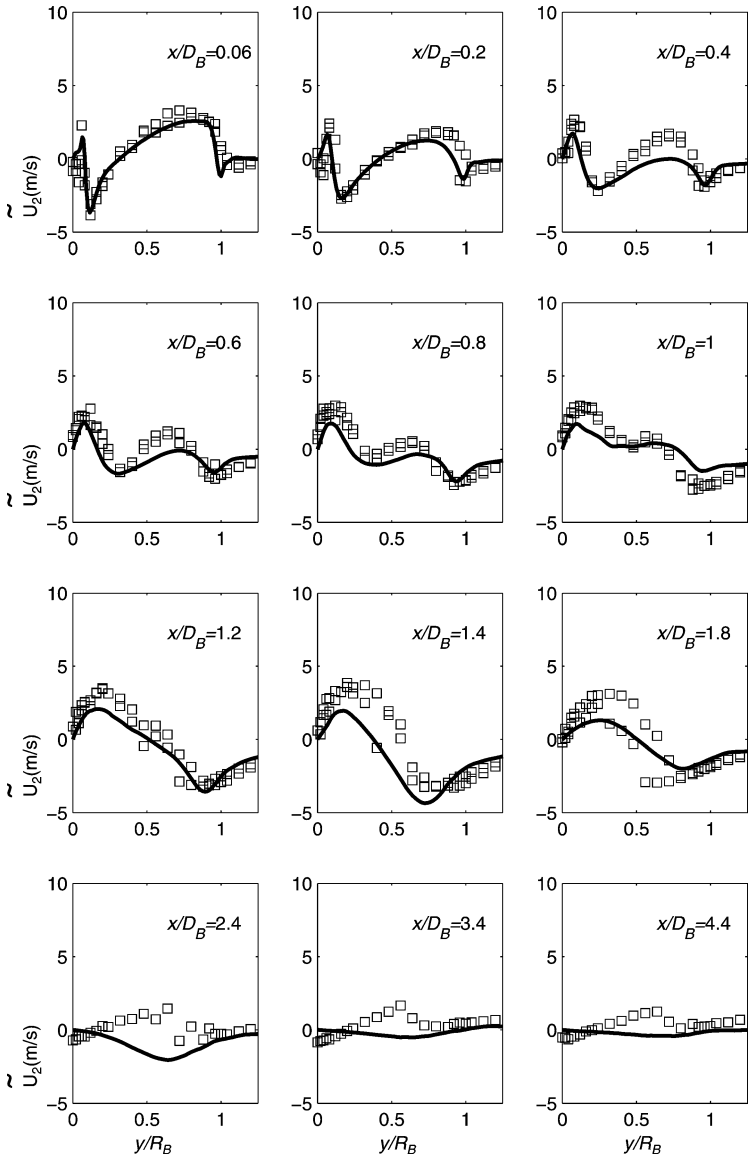

Fig. 11. Radial profiles of the mean radial velocity $\tilde{U}_2$. Symbols, experimental data [9]; lines, joint PDF calculations with IEM mixing model and flamelet chemistry model.

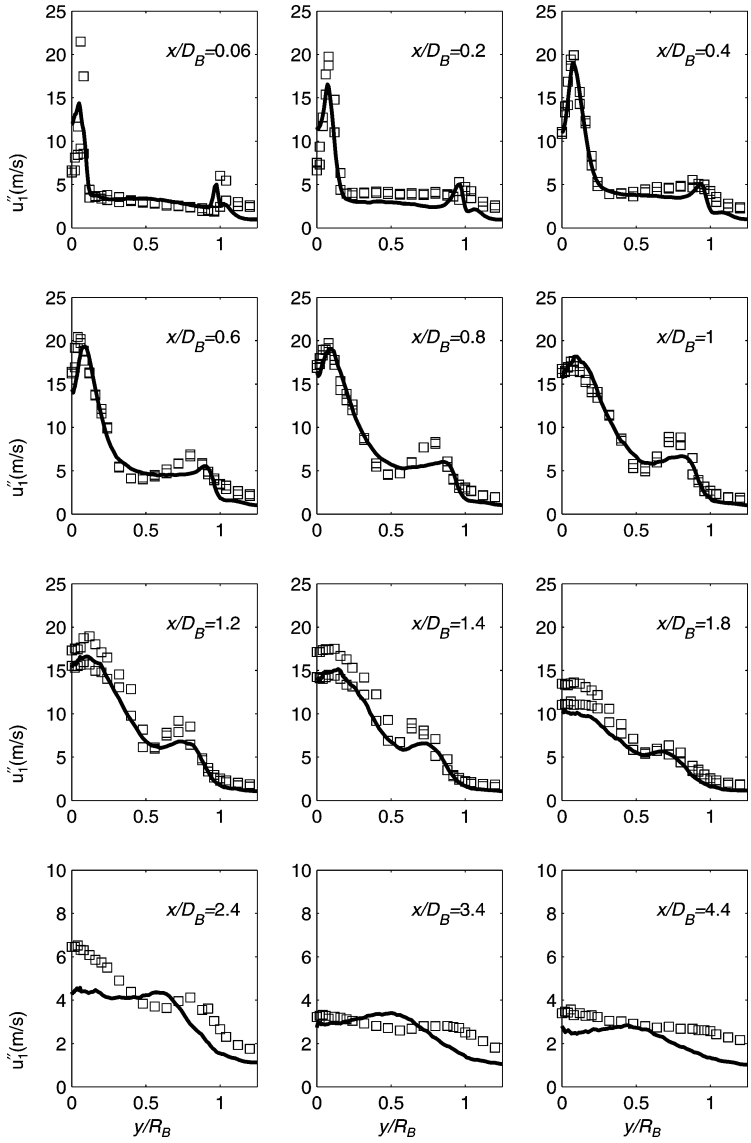

Fig. 12. Radial profiles of the r.m.s. of axial velocity u_1''. Symbols, experimental data [9]; lines, joint PDF calculations with IEM mixing model and flamelet chemistry model.

zone, up to $x/D_{\mathrm{B}} = 1.4$. The agreement deteriorates at downstream locations, which are the neck zone and the jetlike zone, starting from about $x/D_{\mathrm{B}} = 1.8$. Both the shape and the peak values of the radial profiles of the mean axial velocity $\tilde{U}_1$ are well captured within the recirculation zone, but the agreement deteriorates downstream. The mean axial velocity on the centerline for $x/D_{\mathrm{B}} \geqslant 1.4$ decreases more rapidly than in the experimental data. The magnitude of mean radial velocity $\tilde{U}_2$ is one order of magnitude smaller than the axial velocity $\tilde{U}_1$. The agreement between the joint PDF calculations and the experimental data is reasonable for most of the radial velocity profiles. But at the downstream locations, from $x/D_{\mathrm{B}} = 2.4$, where the flow is in the jetlike zone, the profiles are different. Considering that the values of $\tilde{U}_2$ are very small, about 2 m/s, the discrepancies in these profiles are not as significant as they may appear. The agreement between the profiles of r.m.s. velocities is very good up to the location $x/D_{\mathrm{B}} = 1.4$. The discrepancy of the higher peak in the profiles at the first one or two axial locations may be due to the high uncertainty of the experimental data [9]. Again, the agreement in the jetlike zone ($x/D_{\mathrm{B}} \geqslant 2.4$) deteriorates (even the shape is different) although the values become smaller and smaller.

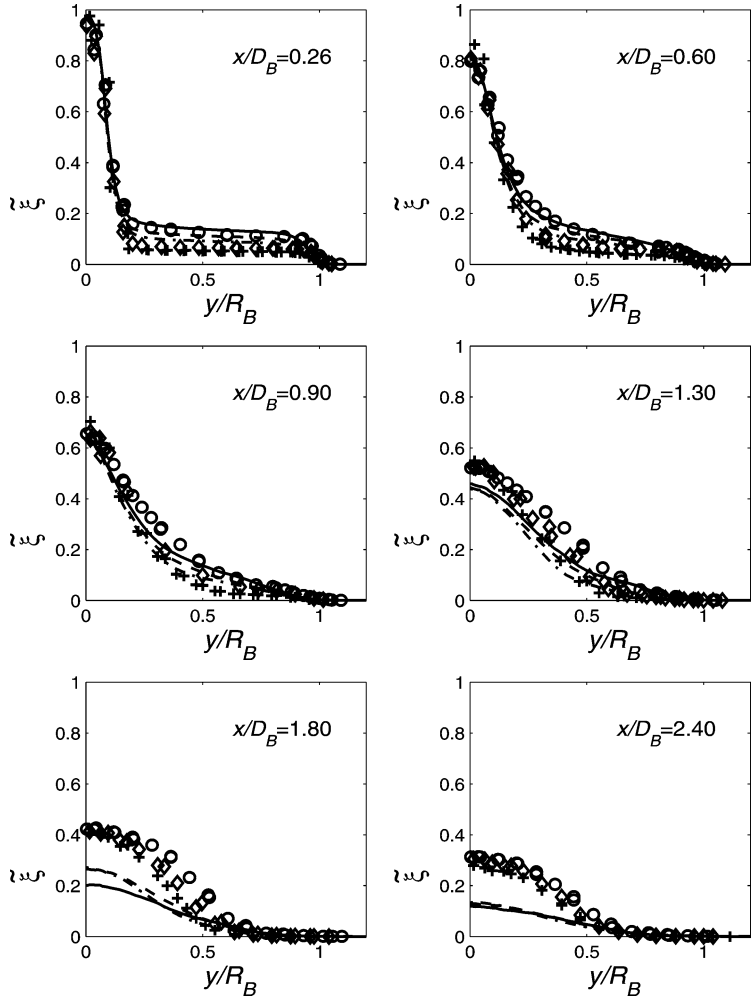

Fig. 13. Radial profiles of mean mixture fraction: HM1 (experiment, ○; joint PDF, solid line), HM2 (experiment, ◇; joint PDF, dashed line), and HM3 (experiment, +; joint PDF, dash-dotted line).

Deterioration in the agreement between the model calculations and the experimental data in the neck zone was also observed in the RSM and k–ε turbulence model calculations shown in the TNF workshops [28]. The reason for these discrepancies is still not clear.

5.2. Mean composition fields

The joint velocity–composition–turbulence frequency PDF method implemented in the hybrid FV/Monte Carlo particle algorithm is applied to bluff-body flames HM1, HM2, and HM3. The results of the joint PDF calculations are extensively compared with the experimental data from the University of Sydney [9]. The current joint velocity–composition–turbulence frequency PDF calculations are based on the EMST mixing model [21] and the ARM2 methane oxidation mechanism [23], which is implemented using the ISAT algorithm [20]. The value of the mixing model constant C_ϕ is varied from 1.0 to 2.0 to investigate its influence on calculations of the turbulence–chemistry interaction. The base case calculations are performed with $C_\phi = 1.5$, as recommended by Xu [33]. The ISAT error tolerance is $\varepsilon_{\text{tol}} = 10^{-4}$. All calculations in this subsection are on the 72×96-cell Grid C (see Section 4.4).

The time-averaged scalar fields are compared with the experimental data for HM1, HM2, and HM3 flames together.

The radial profiles of the mean and r.m.s. of mixture fraction are shown in Figs. 13–15 at six axial locations. For the profiles of mean mixture fraction, agreement between joint PDF calculations and experimental data is reasonable for HM1, but less so for HM2 and HM3, especially in the recirculation zone,

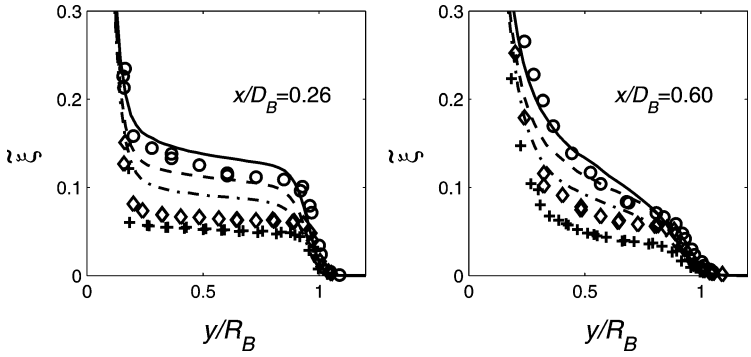

Fig. 14. Radial profiles of mean mixture fraction (expanded view in recirculation zone). HM1 (experiment, ○; joint PDF, solid line), HM2 (experiment, ◇; joint PDF, dashed line), and HM3 (experiment, +; joint PDF, dash-dotted line).

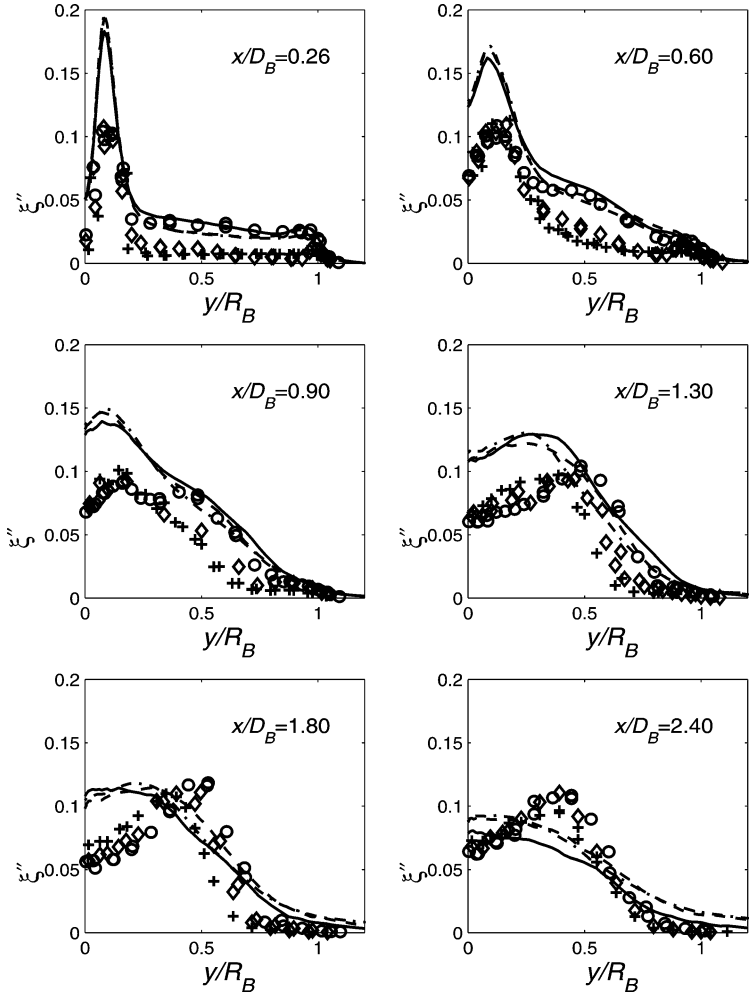

Fig. 15. Radial profiles of r.m.s. of mixture fraction: HM1 (experiment, ○; joint PDF, solid line), HM2 (experiment, ◇; joint PDF, dashed line), and HM3 (experiment, +; joint PDF, dash-dotted line).

and deteriorates downstream. Fig. 14 is a more detailed view of the mean mixture fraction profiles in the recirculation zone. As may be seen, the calculations for flame HM1 are quite accurate. But for flames HM2 and HM3, the calculations do not represent accurately the substantially reduced values of mixture

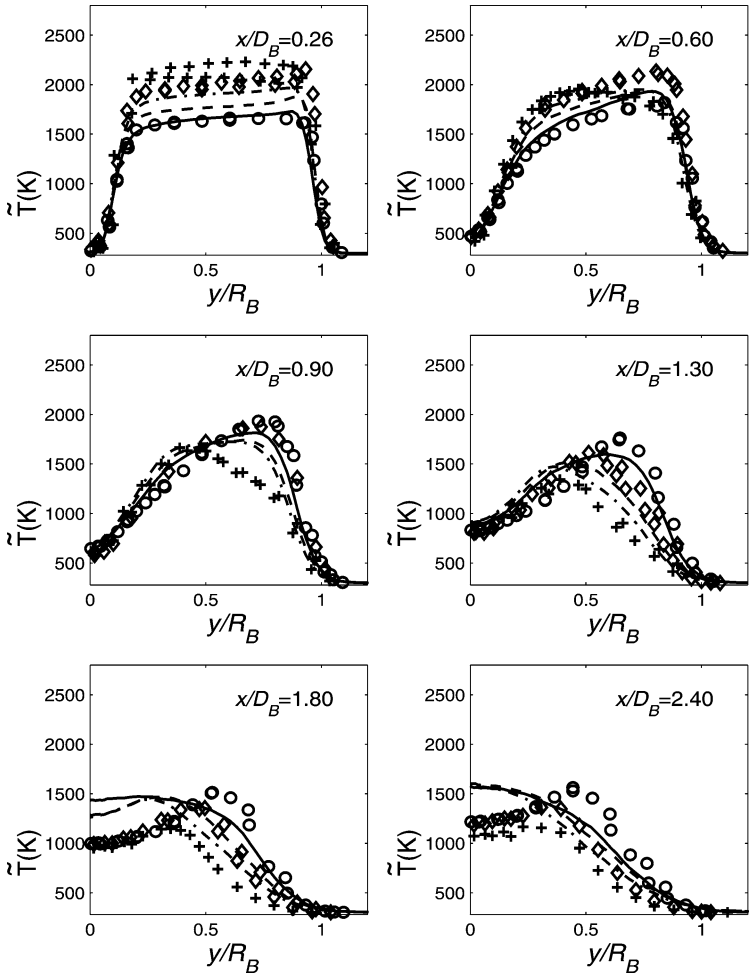

Fig. 16. Radial profiles of Favre mean temperature: HM1 (experiment, ○; joint PDF, solid line), HM2 (experiment, ◇; joint PDF, dashed line), and HM3 (experiment, +; joint PDF, dash-dotted line).

fraction observed in the measurements. The values measured at $x/D_B = 0.26$ are around stoichiometric ($\xi_{st} \approx 0.050$), whereas the calculations are about twice this value. This is a serious discrepancy which is most likely responsible for the discrepancies (reported below) in other calculated quantities in flames HM2 and HM3.

The profiles of the r.m.s. of mixture fraction capture the shape of the experimental data for $x/D_B \leqslant 1.3$, but the peak values of the profiles and the centerline values are overpredicted for all three flames. A comparison of the three flames shows that, as with the mean mixture fraction, the r.m.s. of mixture fraction decreases in the recirculation zone as the jet velocity increases from HM1 to HM3, but the extent of this effect is not reproduced in the PDF calculations.

As may be seen from Fig. 16, for flame HM1, agreement between the calculated and measured mean temperatures is quite good as far downstream as $x/D_B = 1.30$, but it deteriorates further downstream, especially close to the centerline. At the first location ($x/D_B = 0.26$) the experimental data show the mean temperature increasing from flame HM1 to HM2 to HM3. This occurs as a result of the mixture fraction in the recirculation zone decreasing with increasing jet velocity, and being close to stoichiometric for flame HM3 (see Fig. 14). The calculations show the same trends, but the magnitude of the effect is considerably less both for mixture fraction and for temperature. Thus, the discrepancy in the calculated mean temperature at $x/D_B = 0.26$ for flame HM2, and particularly for flame HM3, can be attributed primarily to the discrepancy in mixture fraction. At $x/D_B = 1.30$ the calculations provide a better prediction of the mean temperature differences between the three flames. Comparing the three flames, from HM1 to HM3, the mean temperature increases at the

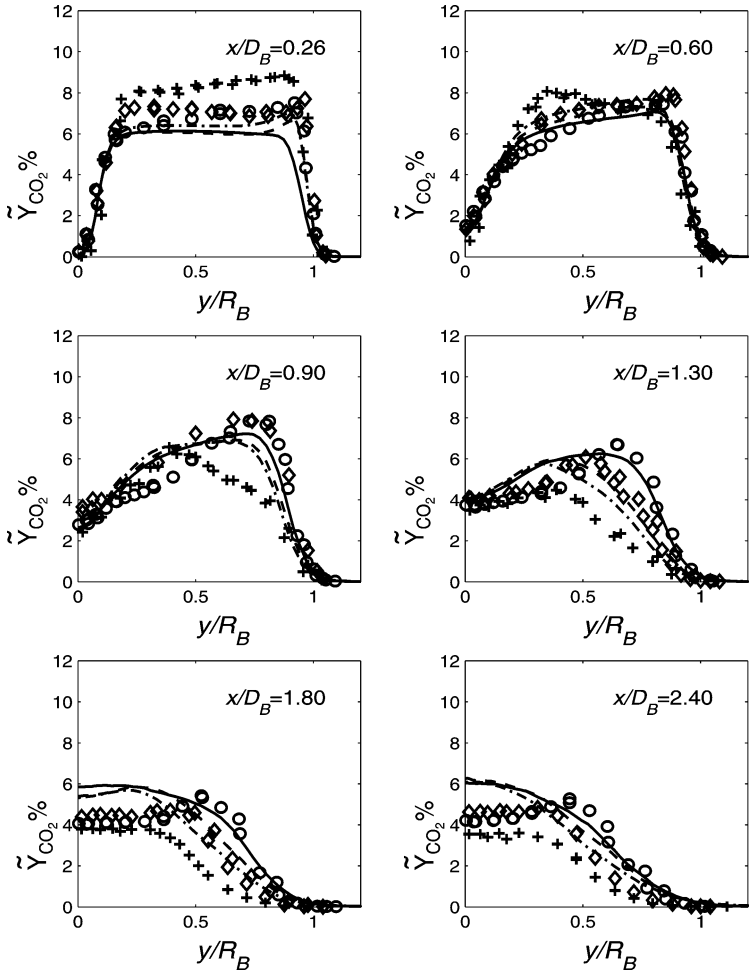

Fig. 17. Radial profiles of Favre mean mass fraction of CO_2: HM1 (experiment, ○; joint PDF, solid line), HM2 (experiment, ◇; joint PDF, dashed line), and HM3 (experiment, +; joint PDF, dash-dotted line).

first two axial locations and decreases at the other four downstream locations. At these downstream locations, as the temperatures of HM2 and HM3 are obviously lower than that of HM1, a greater amount of local extinction occurs (which is clearly shown in the scatterplots below).

The radial time-averaged Favre-averaged mean profiles of the mass fractions of species CO_2, CO, OH, and NO are shown in Figs. 17–20.

For CO_2 (Fig. 17) the trends are similar to those of mean temperature: at $x/D_B = 0.26$, $\tilde{Y}_{CO_2}$ increases from HM1 to HM2 to HM3, whereas at $x/D_B = 1.30$, this trend is reversed. The calculations reproduce these trends qualitatively, but not quantitatively.

For CO (Fig. 18), for HM1 and HM2, the agreement between calculations and measurements is quite good (at least for $x/D_B \leqslant 1.80$). A striking observation from the experimental data is the different behavior of flame HM3 at the first three axial locations. The mean CO concentrations in the experimental data for HM3 are much smaller than those in HM1 and HM2. This behavior is not reproduced by the calculations.

Similar comments apply to OH (Fig. 19). For HM1 and HM2 the agreement is quite good, with the calculations showing the correct trends. But the different behavior of flame HM3 at $x/D_B = 0.26$ and 0.60 is not well reproduced in the calculations.

For all three flames, NO (Fig. 20) is overpredicted at almost all locations. Part of the reason is likely to be the inaccuracy of ISAT with the error tolerance used (as discussed in Section 4.6). Comparing all three flames, NO increases at the first three axial locations and decreases at the last three axial locations as the jet velocity increases from HM1 to HM3 both in the measurements and in the calculations. Because of local extinction, the measured profiles of NO in HM3

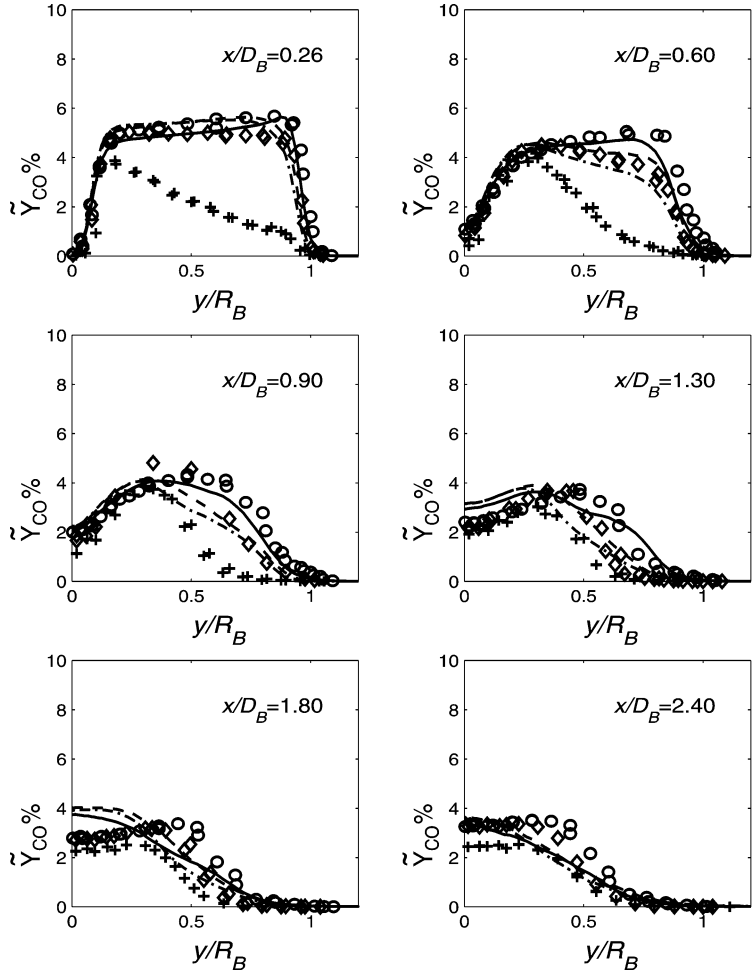

Fig. 18. Radial profiles of Favre mean mass fraction of CO: HM1 (experiment, ○; joint PDF, solid line), HM2 (experiment, ◇; joint PDF, dashed line), and HM3 (experiment, +; joint PDF, dash-dotted line).

drop quickly for $x/D_B \geqslant 0.90$. The current results of the joint PDF calculations do not capture this behavior.

5.3. Scatterplots

Scatterplots are compared with experimental data for flames HM1 and HM3 in Figs. 21–24; the means conditional on mixture fraction are also shown in the figures. The conditional means are calculated for 50 bins equally distributed within mixture fraction space, in the range $[0.0, 1.0]$. The lines for the laminar flamelet model are also shown for reference.

Scatterplots of temperature for HM1 compared with experimental data are shown in Figs. 21 and 22. The radial dependence of the scatterplots may be observed. At the first axial location, $x/D_B = 0.26$, there is nonreactive mixing between the coflow and outer vortex, within the range from $y/R_B = 0.92$ to $y/R_B = 1.0$, whereas within the vortex, $y/R_B < 0.92$, the flame is burning. For the downstream locations, the agreement between calculations and experiment is good. The data bands (the data range at a given mixture fraction) in the joint PDF calculations are narrower than those of experimental data, which is consistent with previous observations [19,33] and is explained in [33].

Scatterplots for HM3 are shown in Figs. 23 and 24. First, in contrast to HM1, nonreactive mixing is not observed in the outer shear layer at the first axial location, $x/D_B = 0.26$, either in the experiments or in the calculations. When we look at the mean mixture fraction profiles in Fig. 14, we find that, outside the recirculation zone at the axial location $x/D_B = 0.26$ (the outer end of the plateau in the profiles), the mean mixture fraction for the three flames is different. For HM1, the value of $\tilde{\xi}$ is about 0.1; for HM2 and HM3,

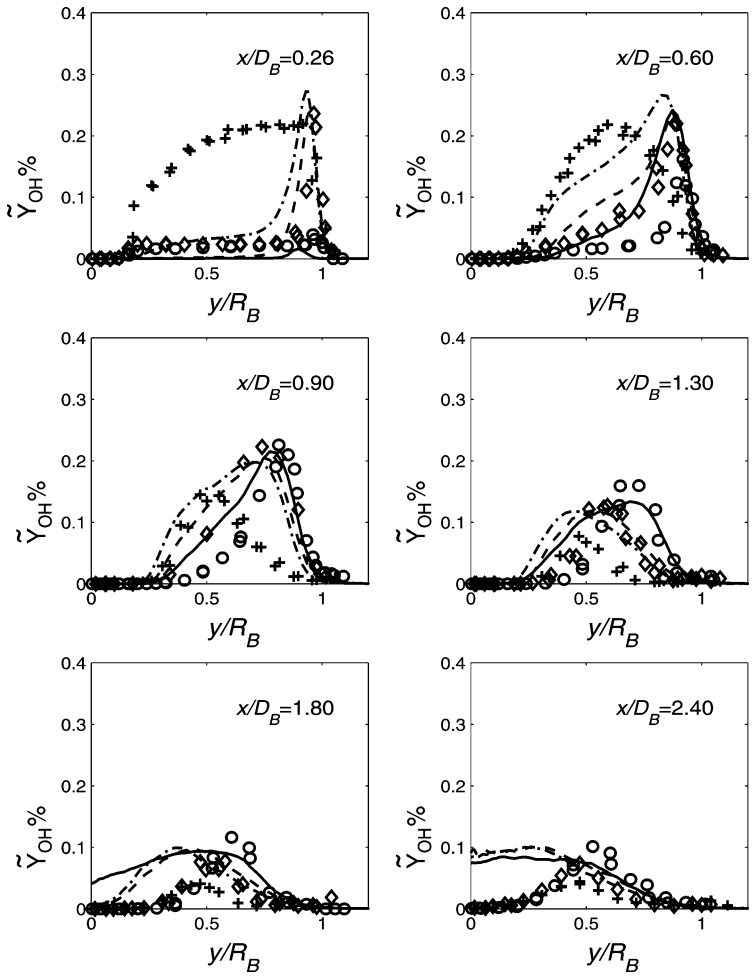

Fig. 19. Radial profiles of Favre mean mass fraction of OH: HM1 (experiment, ○; joint PDF, solid line), HM2 (experiment, ◇; joint PDF, dashed line), and HM3 (experiment, +; joint PDF, dash-dotted line).

the value is close to $\xi_{st} = 0.050$. Because of the interaction between mixing and finite-rate chemical reaction, small differences in mixture fraction result in totally different burning characteristics. Second, as may be observed from Fig. 24, local extinction is evident in the experimental data at several locations in HM3. But this local extinction is not observed in the current joint PDF calculations, at least in part because of the mean mixture fraction discrepancy in the recirculation zone for flames HM2 and HM3. This is the reason that the calculated radial profiles for HM3 in Figs. 17–20 are much higher than those of the experimental data. Consequently, NO data are overpredicted in the profiles of the HM2 and HM3 flames.

5.4. Effects of mixing model constant

Xu [33] found the prediction of local extinction to be very sensitive to the value of the mixing model constant C_ϕ. Reducing C_ϕ leads to a higher level of local extinction. The effects of the model constant C_ϕ in the EMST mixing model are studied for the HM2 and HM3 flames. Calculations are conducted with $C_\phi = 2.0$, 1.5, and 1.0. Note that the value widely used for C_ϕ is 2.0 and that suggested by [33] for the piloted-jet flames is $C_\phi = 1.5$.

Figs. 25 and 26 show the radial profiles of mean and variance of mixture fraction and temperature and radial profiles of mean mass fraction of species CO_2, CO, OH, and NO together with the experimental data for flame HM2. The effects of the mixing model constant C_ϕ on the mean mixture fraction are very weak, as shown in Fig. 25; whereas it may be observed that the effect of C_ϕ on the r.m.s. of mixture fraction is strong. As C_ϕ decreases, the variance increases, which is consistent with expectation and previous observation [33]. Similar behavior is observed for the r.m.s. of temperature. This is due to the fact that de-

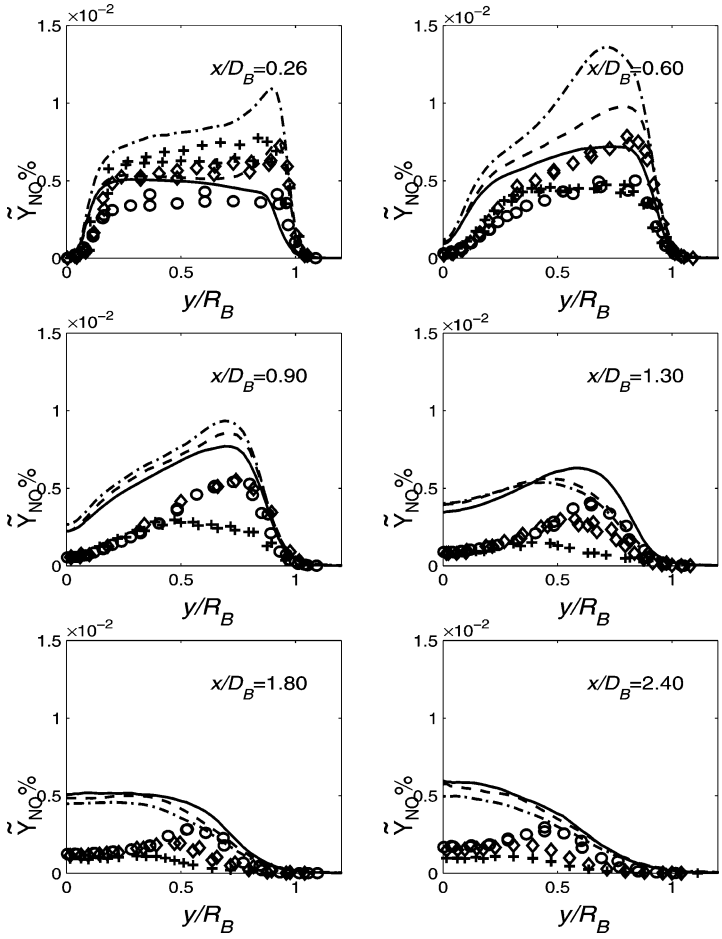

Fig. 20. Radial profiles of Favre mean mass fraction of NO: HM1 (experiment, ○; joint PDF, solid line), HM2 (experiment, ◇; joint PDF; dashed line), and HM3 (experiment, +; joint PDF, dash-dotted line).

creasing C_ϕ increases the time scale of mixing and, thus, decreases the decay rate of variances of scalars. Based on the comparison with experimental data for ξ'', the value $C_\phi = 2.0$ (or even larger) seems "optimal"; but based on T'', the optimal value is $C_\phi = 1.0$. There are no strong effects on the mean temperature profile.

The observations concerning the radial profiles of CO_2 and CO in Fig. 26 are similar to those of temperature. We now examine the effect of C_ϕ on the radical OH. As C_ϕ decreases, the peak value of OH decreases and the profile becomes broader, which indicates that the reaction region is becoming broader. It may be observed that the agreement with experimental data is somewhat better for $C_\phi = 2.0$ than for $C_\phi = 1.5$. The calculated NO profiles with $C_\phi = 2.0$ are seen to be significantly overpredicted when compared with the experimental data. Both OH and NO profiles with $C_\phi = 1.0$ and $C_\phi = 1.5$ are overpredicted and the differences between them are not significant.

5.5. Mean scalar dissipation

The mean scalar dissipation rate, $\tilde{\chi}$, is an important quantity in many approaches to modeling nonpremixed turbulent combustion [28], including the conditional moment closure (CMC) and the flamelet model. The mean scalar dissipation rate is defined by

$$\tilde{\chi} \equiv \langle 2\rho D \nabla\xi \cdot \nabla\xi \rangle / \langle \rho \rangle, \tag{21}$$

and is modeled as

$$\tilde{\chi} = C_\phi \widetilde{\xi''^2} \Omega, \tag{22}$$

where ξ is the mixture fraction, D is its molecular diffusivity, C_ϕ is the mixing model constant, and $\widetilde{\xi''^2}$ is the variance of mixture fraction.

Fig. 27 shows the radial profiles of mean scalar dissipation rate (obtained from Eq. (22)) at several axial locations from the joint PDF calculations with $C_\phi = 1.5$. (No experimental data are available for comparison.) It may be clearly seen that the mean

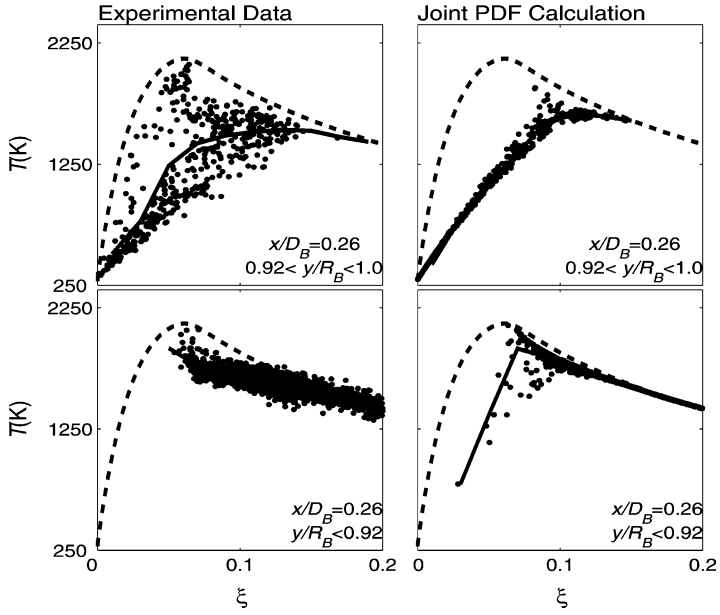

Fig. 21. Scatterplots of temperature against mixture fraction for HM1 at $x/D_{\mathrm{B}} = 0.26$. Upper plots, in outer shear layer; lower plots, in recirculation zone. Left, experimental data; right, joint PDF calculations with $C_\phi = 1.5$. Solid line, conditional mean; dashed line, flamelet.

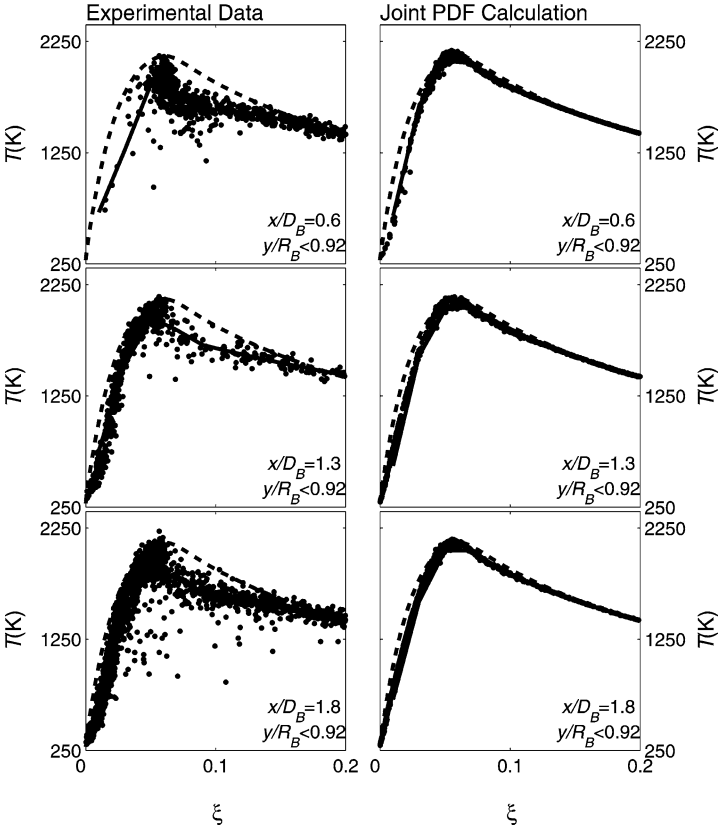

Fig. 22. Scatterplots of temperature against mixture fraction for HM1 at three axial locations. Left, experimental data; right, joint PDF calculations with $C_\phi = 1.5$. Solid line, conditional mean; dashed line, flamelet.

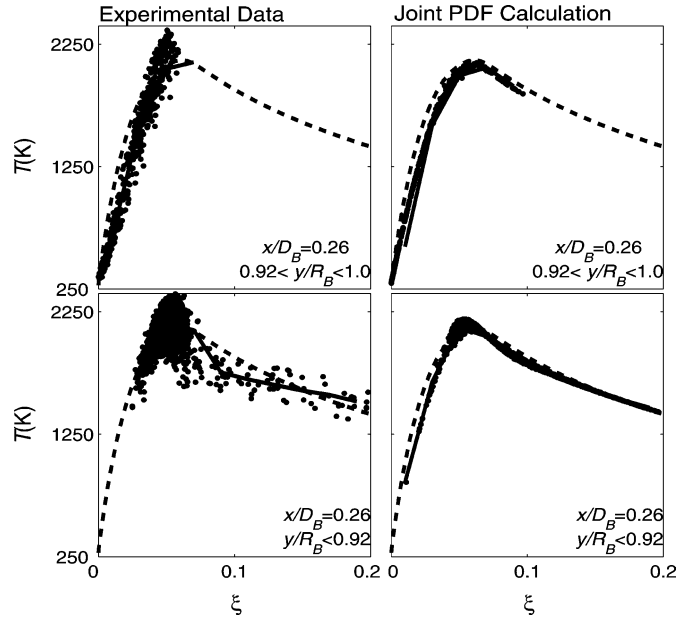

Fig. 23. Scatterplots of temperature against mixture fraction for HM3 at $x/D_{\mathrm{B}} = 0.26$. Upper plots, in outer shear layer; lower plots, in recirculation zone. Left, experimental data; right, joint PDF calculations with $C_\phi = 1.5$. Solid line, conditional mean; dashed line, flamelet.

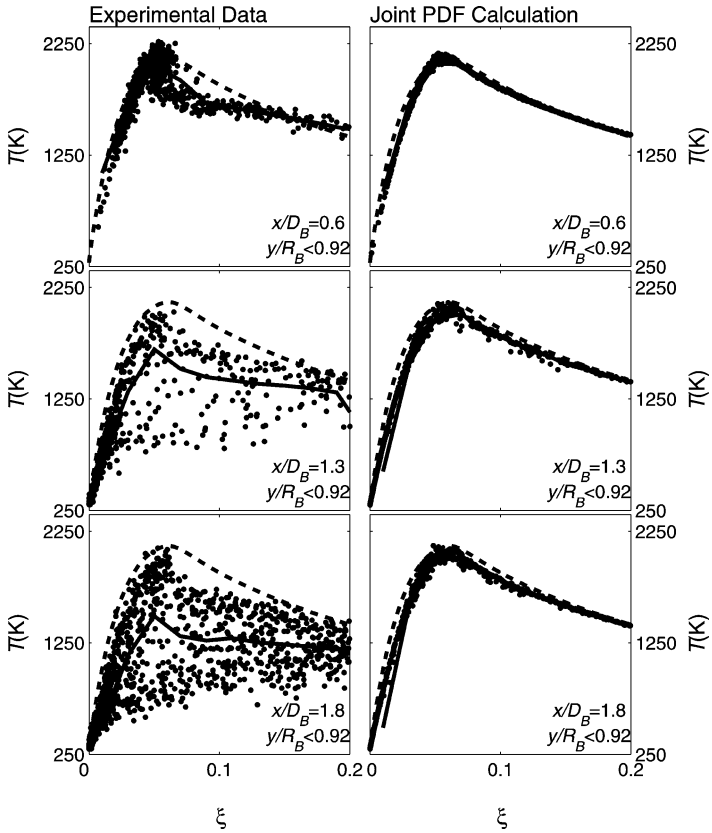

Fig. 24. Scatterplots of temperature against mixture fraction for HM3 at three axial locations. Left, experimental data; right, joint PDF calculations with $C_\phi = 1.5$. Solid line, conditional mean; dashed line, flamelet.

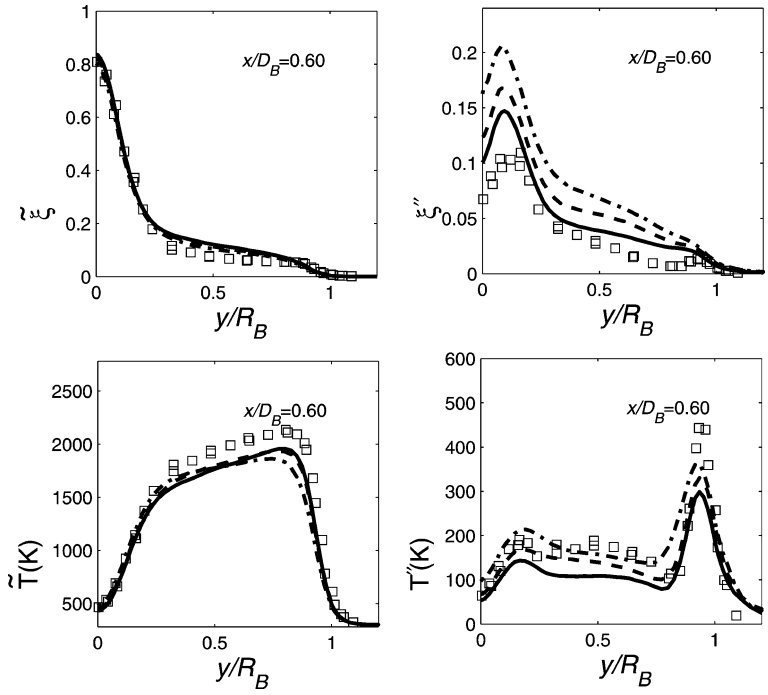

Fig. 25. Effects of the mixing model constant C_ϕ for HM2: radial profiles of Favre mean and r.m.s. of mixture fraction and temperature. Solid lines, $C_\phi = 2.0$; dashed lines, $C_\phi = 1.5$; dash-dotted lines, $C_\phi = 1.0$.

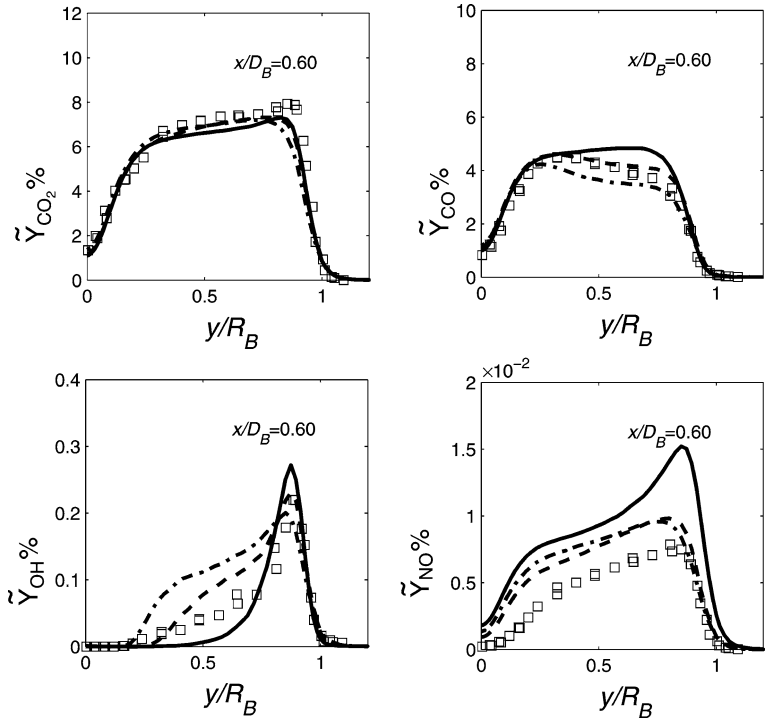

Fig. 26. Effects of the mixing model constant C_ϕ for HM2: radial profiles of Favre mean mass fraction of CO_2, CO, OH, and NO. Solid lines, $C_\phi = 2.0$; dashed lines, $C_\phi = 1.5$; dash-dotted lines, $C_\phi = 1.0$.

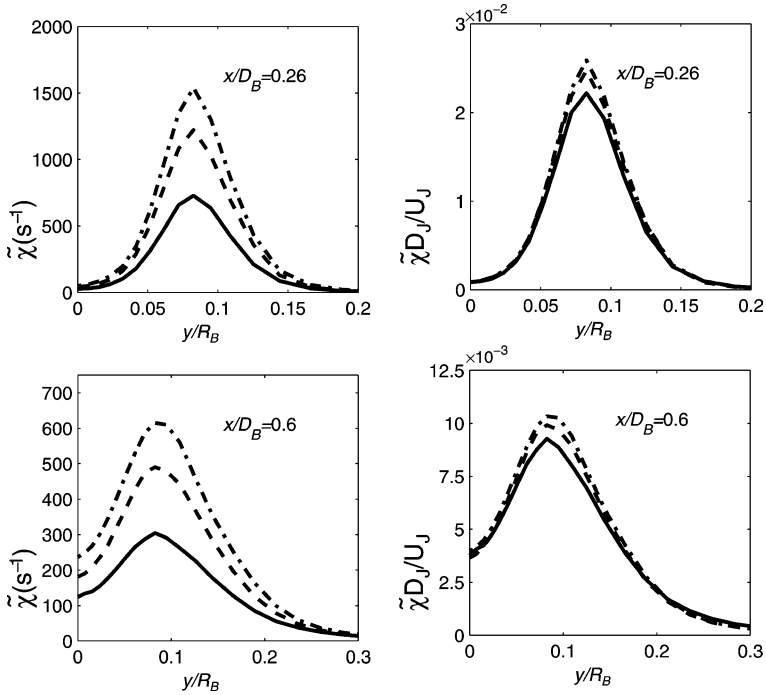

Fig. 27. Radial profiles of mean scalar dissipation rate for flames HM1 (solid lines), HM2 (dashed lines), and HM3 (dash-dotted lines) from joint PDF calculations with $C_\phi = 1.5$.

scalar dissipation rate increases as jet velocity increases (Fig. 27). On the right side of this figure, the mean scalar dissipation rate is normalized as

$$\tilde{\chi}^* = \frac{\tilde{\chi} D_\mathrm{J}}{U_\mathrm{J}}, \tag{23}$$

where $D_\mathrm{J} = 0.0036$ m is the diameter of the jet and U_J is the jet bulk velocity (see Table 1). As expected from a simple scaling argument, there is no significant difference for $\tilde{\chi}^*$ in the three flames.

6. Calculation cost

Typically, a calculation with the EMST mixing model ($N_\mathrm{PC} = 100$ and 6000 particle pseudo-time steps), on a single-processor, 1.8-GHz workstation with 1 GB RAM, requires about 400 h CPU time, of which 50% is used by ISAT. Compared with direct integration, ISAT achieves a speedup of a factor of 400.

7. Conclusions

The joint PDF method implemented as a fully consistent hybrid FV/Monte Carlo particle algorithm is applied to bluff-body stabilized flames, including Sydney [9] flames HM1, HM2, and HM3. Numerical accuracy issues are carefully addressed, including the specification of inlet boundary conditions, grid convergence, and bias error. The ARM2 mechanism for methane implemented by the ISAT algorithm is used for detailed chemistry calculations. Statistically stationary solutions are obtained. Calculations are comprehensively compared with the experimental data. The effects of the mixing model constants are investigated. From this work, conclusions can be drawn as follows.

Numerical accuracy issues for bluff-body stabilized flames are investigated with a simple laminar flamelet chemistry model. The computational domain and boundary conditions are carefully specified such that the calculations are sensitive neither to the current domain size nor to the inlet boundary conditions. Numerical errors in the joint PDF calculations are studied. The bias errors are smaller than 5% for $N_\mathrm{PC} \geqslant 100$. Grid convergence is achieved. On Grid C with 72×96 cells, the spatial discretization errors are smaller than 10% for the mean fields. The spatial discretization errors for the variance fields are not very small but less than 20% for Grid C.

The EMST mixing model and the ARM2 mechanism are used to model flames HM1, HM2, and HM3. Statistically stationary results are obtained. ISAT errors are examined using an autoignition test case. With the ISAT error tolerance $\varepsilon_\mathrm{tol} = 10^{-4}$, the errors from tabulation are controlled within 1% for temperature and major species, and within 5% for CO and

OH, whereas errors for NO may be as large as 30% at some locations.

Most of the calculations are in poor agreement with the experimental data at the far downstream locations, $x/D_B \geqslant 1.80$, and so the remaining conclusions pertain to the upstream region, $x/D_B < 1.80$. For HM1, the agreement for temperature, major species, and minor species CO and OH is generally quite good. For flames HM2 and HM3, the calculations yield larger values of $\tilde{\xi}$ than the experimental results, which are close to stoichiometric in the recirculation zone. As a consequence, the differences in $\tilde{T}$ and $\tilde{Y}_{CO_2}$, for example, between the three flames are not well reproduced in the calculations at the first two axial locations. Overall, $\tilde{Y}_{NO}$ is overpredicted.

In the outer shear layer of flame HM1, there is essentially inert mixing between the coflowing air and the rich combustion products in the recirculation zone, a phenomenon that is reproduced by the calculations, but not observed in flames HM2 and HM3, either in the experimental data or in the calculations. Substantial local extinction is observed in the experimental data for flame HM3, but not reproduced in the current calculations, even after decreasing C_ϕ to 1.0.

Only the EMST mixing model has been used for the detailed chemistry calculations. While it would be worthwhile in future work to evaluate the performance of other mixing models, experience suggests that the use of other mixing models would not remedy the deficiencies of the current calculations.

Acknowledgment

This work was supported by the U.S. Department of Energy under Grant DE-FG02-90ER14128.

References

[1] W.M. Roquemore, R.P. Bradley, J.S. Stutrud, C.M. Reeves, L. Krishnamurthy, ASME Paper 95-GT-307, 1980.
[2] A.R. Masri, R.W. Bilger, Proc. Combust. Inst. 20 (1984) 319–325.
[3] A.R. Masri, R.W. Dibble, R.S. Barlow, Proc. Combust. Inst. 24 (1992) 317–323.
[4] A.R. Masri, B.B. Dally, R.S. Barlow, C.D. Carter, Proc. Combust. Inst. 25 (1994) 1301–1307.
[5] A.R. Masri, J.B. Kelman, B.B. Dally, Proc. Combust. Inst. 27 (1998) 1031–1036.
[6] B.B. Dally, A.R. Masri, R.S. Barlow, G.J. Fiechtner, D.F. Fletcher, Proc. Combust. Inst. 26 (1996) 2191–2196.
[7] B.B. Dally, A.R. Masri, R.S. Barlow, G.J. Fiechtner, Combust. Flame 114 (1998) 119–148.
[8] B.B. Dally, PhD thesis, University of Sydney, Sydney, 1997.
[9] A.R. Masri, http://www.mech.eng.usyd.edu.au/research/energy/#data.
[10] B.B. Dally, D.F. Fletcher, A.R. Masri, Combust. Theory Model. 2 (1998) 193–219.
[11] B. Merci, E. Dick, J. Vierendeels, D. Roekaerts, T.W.J. Peeters, Combust. Flame 126 (2001) 1533–1556.
[12] G.X. Li, D. Roekaerts, B. Naud, Flow Turb. Combust. 70 (2003) 211–240.
[13] M. Hossain, J.C. Jones, W. Malalasekera, Flow Turb. Combust. 67 (2001) 217–234.
[14] S.H. Kim, K.Y. Huh, L. Tao, Combust. Flame 120 (2000) 75–90.
[15] S.H. Kim, K.Y. Huh, Combust. Flame 130 (2002) 94–111.
[16] S.B. Pope, Prog. Energy Combust. Sci. 11 (1985) 119–192.
[17] J. Xu, S.B. Pope, Combust. Flame 123 (2000) 281–307.
[18] R.P. Lindstedt, S. Louludi, T. Vaos, Proc. Combust. Inst. 28 (2000) 149–155.
[19] Q. Tang, J. Xu, S.B. Pope, Proc. Combust. Inst. 28 (2000) 133–139.
[20] S.B. Pope, Combust. Theory Model. 1 (1997) 41–64.
[21] S. Subramaniam, S.B. Pope, Combust. Flame 115 (1998) 487–514.
[22] C.J. Sung, C.K. Law, J.-Y. Chen, Proc. Combust. Inst. 27 (1998) 295–301.
[23] C.J. Sung, C.K. Law, J.-Y. Chen, Combust. Flame 125 (2001) 906–919.
[24] P. Jenny, S.B. Pope, M. Muradoglu, D.A. Caughey, J. Comput. Phys. 166 (2001) 218–252.
[25] M. Muradoglu, S.B. Pope, D.A. Caughey, J. Comput. Phys. 172 (2001) 841–878.
[26] P. Jenny, M. Muradoglu, K. Liu, S.B. Pope, D.A. Caughey, J. Comput. Phys. 169 (2001) 1–23.
[27] M. Muradoglu, K. Liu, S.B. Pope, Combust. Flame 132 (2003) 115–137.
[28] R.S. Barlow, International Workshop on Measurement and Computation of Turbulent Nonpremixed Flames, http://www.ca.sandia.gov/TNF.
[29] R.P. Lindstedt, private communication, 2003.
[30] T.S. Kuan, PhD thesis, Imperial College, London, 2003.
[31] R.W. Bilger, S.H. Starner, R.J. Kee, Combust. Flame 80 (1990) 135–149.
[32] S.B. Pope, Turbulent Flows, Cambridge Univ. Press, Cambridge, 2000.
[33] J. Xu, PhD thesis, Cornell University, Ithaca, NY, 2000.
[34] S.B. Pope, Y.L. Chen, Phys. Fluids A 2 (1990) 1437–1449.
[35] D.C. Haworth, S.B. Pope, Phys. Fluids 29 (1986) 387–405.
[36] S.B. Pope, Phys. Fluids 6 (1994) 973–985.
[37] P.R. Van Slooten, Jayesh, S.B. Pope, Phys. Fluids 10 (1998) 246–265.
[38] J. Villermaux, J.C. Devillon, in: Proceedings: Second International Symposium on Chemical Reaction Engineering, 1972.
[39] J. Janicka, W. Kolbe, W. Kollmann, J. Non-Equilib. Thermodyn. 4 (1977) 47–66.

[40] Z. Ren, S. Subramaniam, S.B. Pope, http://mae.conrell.edu/~laniu/emst, Cornell University.
[41] D.B. Spalding, Chem. Eng. Sci. 26 (1971) 95.
[42] J. Xu, S.B. Pope, Report FDA 99-06, Cornell University, 1999.
[43] A.R. Masri, private communication, 1999.
[44] M. Muradoglu, PhD thesis, Cornell University, Ithaca, NY, 2000.
[45] K. Liu, PhD thesis, Cornell University, Ithaca, NY, 2004.
[46] J. Xu, S.B. Pope, J. Comput. Phys. 152 (1999) 192–230.